JEM Journal of Experimental Medicine

ARTICLE

The germinal center reaction depends on RNA methylation and divergent functions of specific methyl readers

Amalie C. Grenov[1], Lihee Moss[1], Sarit Edelheit[2], Ross Cordiner[3], Dominik Schmiedel[1], Adi Biram[1], Jacob H. Hanna[2], Torben Heick Jensen[3], Schraga Schwartz[2], and Ziv Shulman[1]

Long-lasting immunity depends on the generation of protective antibodies through the germinal center (GC) reaction. *N*^{6}-methyladenosine (m^{6}A) modification of mRNAs by METTL3 activity modulates transcript lifetime primarily through the function of m^{6}A readers; however, the physiological role of this molecular machinery in the GC remains unknown. Here, we show that m^{6}A modifications by METTL3 are required for GC maintenance through the differential functions of m^{6}A readers. Mettl3-deficient GC B cells exhibited reduced cell-cycle progression and decreased expression of proliferation- and oxidative phosphorylation–related genes. The m^{6}A binder, IGF2BP3, was required for stabilization of *Myc* mRNA and expression of its target genes, whereas the m^{6}A reader, YTHDF2, indirectly regulated the expression of the oxidative phosphorylation gene program. Our findings demonstrate how two independent gene networks that support critical GC functions are modulated by m^{6}A through distinct mRNA binders.

Introduction

The adaptive immune response has the capacity to generate long-lasting immunological memory that provides a rapid response to recurrent pathogen exposures (Ahmed and Gray, 1996; Tarlinton and Good-Jacobson, 2013; Cyster and Allen, 2019). The primary goal of vaccination is to induce the generation of long-lived antibody-forming cells through the activation of the humoral arm of the adaptive immune response (Corcoran and Tarlinton, 2016; Plotkin, 2008; Ise and Kurosaki, 2019). High-affinity antibodies are secreted by plasma cells (PCs), which typically originate from germinal centers (GCs), microanatomic sites in lymphoid organs where B cells proliferate extensively and accumulate somatic hypermutations (SHMs) in their Ig genes (Victora and Nussenzweig, 2012; Shlomchik and Weisel, 2012; Cyster 2010; De Silva and Klein, 2015; Berek, 1992; MacLennan, 1994; Jacob et al., 1991). The selection of high-affinity clones for preferential expansion in the GC is mediated primarily by helper T cells (Vinuesa and Cyster, 2011; Victora et al., 2010; Crotty, 2011). In this process, the degree of T cell–derived signals induces corresponding expression levels of MYC in GC B cells, which in turn activates downstream cell cycle and metabolic gene programs (Gitlin et al., 2014; Gitlin et al., 2015; Finkin et al., 2019; Calado et al., 2012; Dominguez-Sola et al., 2012; Monzón-Casanova et al., 2018; Ersching et al., 2017; Chou et al., 2016). *Myc* is an immediate-early gene that rapidly produces mRNA transcripts with an extremely short half-life in response to mitogenic signals (Jones and Cole, 1987; Dani et al., 1984). Although GC B cells rapidly divide, their metabolic program is very different from that of other proliferating lymphocytes (Weisel et al., 2020). Whereas activated T and B cells can consume glucose and generate acetyl-CoA through glycolysis, GC B cells primarily oxidize fatty acids in the mitochondria and peroxisomes for respiration (Weisel et al., 2020; Vander Heiden et al., 2009).

Immune cell differentiation and acquisition of effector functions depend on extensive changes in gene expression that are regulated by transcriptional and post-transcriptional machineries (Turner and Díaz-Muñoz, 2018). The addition of a methyl group at position N6 on adenosines (*N*^{6}-methyladenosine [m^{6}A]) is the most abundant post-transcriptional modification in mammalian mRNA (Shulman and Stern-Ginossar, 2020; Zaccara et al., 2019). This process is mediated by an mRNA-modifying complex that includes METTL3, a methyltransferase that catalyzes the addition of m^{6}A at consensus sites (Zaccara et al., 2019; Shulman and Stern-Ginossar, 2020). The functional

[1]Department of Immunology, Weizmann Institute of Science, Rehovot, Israel; [2]Department of Molecular Genetics, Weizmann Institute of Science, Rehovot, Israel; [3]Department of Molecular Biology and Genetics, Aarhus University, Aarhus, Denmark.

Correspondence to Ziv Shulman: ziv.shulman@weizmann.ac.il.

consequence of this complex activity is determined by m^{6}A-binding proteins that interact with the modified mRNA and modulate its half-life, location, splicing, and translation rate (Shi et al., 2019; Shi et al., 2017). Typically, m^{6}A modifications promote mRNA destabilization, primarily through the binding of the m^{6}A-interacting proteins, YTH domain–containing family proteins 1, 2, and 3 (YTHDF1–3), in the cytosolic compartment (Ivanova et al., 2017; Du et al., 2016; Wang et al., 2014; Shi et al., 2017; Zaccara and Jaffrey, 2020). Conversely, the family of IGF2 mRNA-binding proteins (BPs) 1, 2, and 3 (aka IMP1–3) stabilize transcripts and prolong their lifetimes (Palanichamy et al., 2016; Ren et al., 2020; Dai, 2020). RNA modifications by METTL3 augment the binding capacity of IGF2BP paralogs to mRNAs, resulting in the stabilization of several methylated transcripts, including DNA replication– and cell cycle–related genes (Sun et al., 2019; Huang et al., 2018; Müller et al., 2020). IGF2BP3 is the major paralog expressed in immune cells, yet its physiological functions remain unknown.

The m^{6}A molecular machinery was found to play a critical role in supporting the adaptive immune response, including in differentiation of T follicular helper cells that provide help to B cells in GCs (Li et al., 2017; Zheng et al., 2020; Bechara et al., 2021; Ma et al., 2021; Yao et al., 2021). Here, we examined how RNA methylation and m^{6}A binders regulate the expression of gene programs that support the generation and persistence of GC B cells. We found that effective cell cycle progression, GC formation, and persistence depend on METTL3 functions. The m^{6}A interactor, IGF2BP3, is required for GC persistence by supporting *Myc* transcript stabilization and downstream pathways, whereas the m^{6}A reader, YTHDF2, governs the proper gene expression and function of mitochondrial respiration. Thus, integration of mRNA modulation events by distinct m^{6}A readers supports genetic programs that are critical for effective GC reactions.

Results

GC formation depends on METTL3

To examine whether METTL3 is required for generation and maintenance of the GC reaction, we crossed a Mettl3$^{fl/fl}$ mouse strain to a mouse that expresses Cre recombinase under the B cell–specific CD19 promoter (abbreviated as CD19-Mettl3$^{fl/fl}$); Mettl3$^{fl/+}$ mice that express the Cre recombinase were used as controls. Since CD19 is expressed by B cells during their generation in the bone marrow (BM), we first examined whether B cell development and establishment of the mature B cell compartment is defective in the CD19-Mettl3$^{fl/fl}$ mouse model. Analysis of the different B cell populations in the BM and spleen revealed only minor and insignificant alterations in B cell development in this mouse model (Fig. S1, A and B). Whereas the frequency of mature B cells was normal in these mice, reduced levels of Igs were observed in their serum under homeostatic conditions, suggesting a defect in the ability of Mettl3-deficient B cells to mount an effective immune response (Fig. 1 A). To examine whether METTL3 functions are required for the generation of GC B cells, control and CD19-Mettl3$^{fl/fl}$ mice were immunized subcutaneously in the hind footpads with a hapten (4-hydroxy-3-nitrophenyl [NP]) coupled to keyhole limpet hemocyanin (KLH) in alum, and the presence of GC B cells was examined in the popliteal LNs after 7 d. Flow cytometric analysis revealed that the frequency of GC B cells was fourfold reduced in CD19-Mettl3$^{fl/fl}$ mice compared with controls on day 7 of the response (Fig. 1 B). Furthermore, the frequencies of PCs and memory B cells in the LNs of the CD19-Mettl3$^{fl/fl}$ mice were significantly lower compared with littermate controls (Figs. 1 B and S1 C).

To completely exclude the possibility that defects in GC formation are a result of aberrant B cell development in the BM of CD19-Mettl3$^{fl/fl}$ animals (Zheng et al., 2020), we took an additional approach. CD23 is expressed on B cells in the spleen after their maturation and departure from the BM. Analysis of the B cell immune response in Mettl3$^{fl/fl}$ mice that were crossed to a B cell–specific CD23-Cre mouse strain (CD23-Mettl3$^{fl/fl}$; Kwon et al., 2008) showed complete elimination of GC and PC formation 7 d after immunization (Fig. 1 C). Moreover, immunohistochemistry analysis revealed that GC structures in CD23-Mettl3$^{fl/fl}$ mice were absent (Fig. 1 D). Importantly, diminished Mettl3 mRNA and protein expression was detected in B cells derived from these mice (Fig. S1, D and E). Furthermore, the observed defects were specific for activated B cells, as the frequency of mature naive B cells in LNs was intact (Fig. S1 F). To determine whether early B cell activation or GC seeding was dependent on METTL3 functions, we immunized CD19-Mettl3$^{fl/fl}$ mice with PE, a multi-epitope fluorescent antigen that allows detection of rare antigen-specific B cells in a polyclonal cell population at early time points (Pape et al., 2011). Flow cytometric analysis revealed a major defect in expansion of PE-specific B cells and in upregulation of the early activation markers, CCR6 and FAS, in CD19-Mettl3$^{fl/fl}$ mice 3 d after immunization (Fig. 1, E and F; Schwickert et al., 2011). These experiments demonstrate that METTL3 is essential for initial B cell functions before GC formation.

The findings obtained using CD23-Cre and CD19-Cre mouse models suggest that METTL3 is required for early B cell activation. Overnight stimulation with anti-IgM of B cells derived from UBC^{CreERT2}-Mettl3$^{fl/fl}$ mice and treated with tamoxifen (4OHT) showed no defects in CD86 expression, and B cells from CD23-Mettl3$^{fl/fl}$ mice showed no defect in ERK phosphorylation (pERK) upon activation (Fig. S1, G and H). Yet, these cells proliferated significantly less than control B cells in vitro (Fig. S1 I). Collectively, we conclude that METTL3 plays a critical role in B cell proliferation, but not in their initial activation.

METTL3 is required for GC maintenance

Deletion of *Mettl3* in naive B cells did not allow evaluation of m^{6}A functions in the GC response. Activation-induced cytidine deaminase (AID, encoded by *Aicda*) is expressed in B cells after they encounter cognate antigen, but before GC seeding (Roco et al., 2019; Rommel et al., 2013; Crouch et al., 2007). To examine the functional role of METTL3 after the initial activation events, we crossed Mettl3$^{fl/fl}$ mice to an Aicda$^{Cre/+}$ mouse strain (AID-Mettl3$^{fl/fl}$). In these mice, in the absence of immunological challenge, serum IgG titers but not IgM titers were lower compared with controls, suggesting that effective mounting of

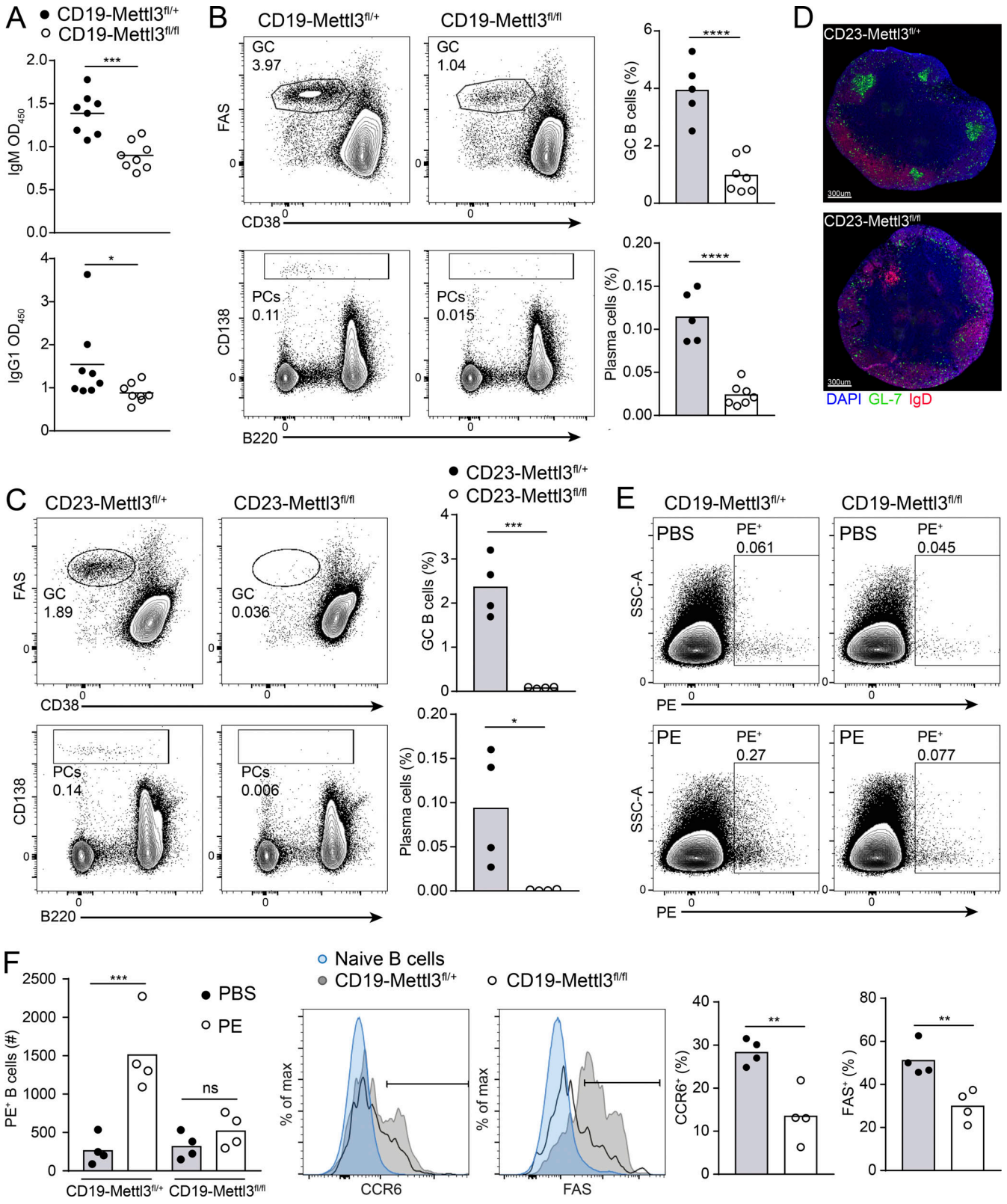

Figure 1. **Mettl3-deficient B cells do not form GCs. (A)** Serum Ig titers of IgM and IgG1 in unmanipulated CD19-Mettl3$^{fl/+}$ or CD19-Mettl3$^{fl/fl}$ mice. 8–10 mice per condition, Student's paired *t* test between age-matched mice was used to determine significance. Lines represent the mean. **(B and C)** The frequency of GC B cells and PCs in control, CD19-Mettl3$^{fl/fl}$ (B), or CD23-Mettl3$^{fl/fl}$ (C) mice, 7 d after NP-KLH immunization. Each data point represents a single mouse, and each column represents the mean value. Pooled data from three experiments with four to seven mice per experiment. **(D)** Representative immunostained slides of popliteal LNs derived from control or CD23-Mettl3$^{fl/fl}$ mice. **(E and F)** Frequency and activation marker expression of naive PE-specific B cells in CD19-Mettl3$^{fl/+}$ or CD19-Mettl3$^{fl/fl}$ 3 d after immunization with PE. Each data point represents a single mouse, and each column indicates the mean value. Pooled data from two experiments each with two mice per condition. SSC, side scatter. *, P < 0.05; **, P < 0.01; ***, P < 0.005; ****, P < 0.001; two-tailed Student's *t* test (A–E) or one-way ANOVA corrected for multiple comparisons (Sidak; F).

antibody immune responses was defective (Fig. S2 A). As opposed to the observations in CD19-Mettl3$^{fl/fl}$ mice, *Mettl3* deletion at the time of AID expression did not affect GC seeding, and the frequencies of GC B cells, PCs, and IgG1^{+} memory cells 7 d after immunization were intact (Figs. 2 A and S2 B). However, after an additional week, the frequencies of these cell populations in AID-Mettl3$^{fl/fl}$ mice were severely reduced compared with control mice (Figs. 2 A and S2 B). The proportion of class-switched IgG1^{+} cells among Mettl3-deficient and control GC B cells was similar (Fig. S2 C). Analysis of *Mettl3* mRNA by quantitative RT-PCR (RT-qPCR) and TdTomato expression in GC B cells revealed effective Cre-mediated recombination in this mouse model, when analyzed 7 and 14 d after immunization (Fig. S2, D and E). Some deficiencies in molecular machineries in B cell immune responses can be detected only under competitive pressure (Zaretsky et al., 2017). To examine whether METTL3 provides a competitive advantage in the GC reaction, we generated mixed BM chimeric mice that host control- and AID-Mettl3$^{fl/fl}$–derived immune cells. In these mice, the frequency of Mettl3-deficient and -proficient B cells in the GC was similar to that of naive B cells on day 7 after immunization (Fig. 2 B), suggesting that even under selective pressure, METTL3 expression did not endow a competitive advantage at this time point. However, after an additional 7 and 14 d, the frequency of GC Mettl3-deficient B cells was strongly reduced, similarly to that observed under noncompetitive conditions (Fig. 2 B). Thus, since the control B cells did not outcompete Mettl3-deficient B cells and since the latter diminished over time regardless of competition, we conclude that the observed defects in AID-Mettl3$^{fl/fl}$ mice are B cell intrinsic. Furthermore, very few Mettl3-deficient B cells were detected in chronic GCs within the Peyer's patches (PPs) of the chimeric mice (Fig. S2 F). Since GCs in PPs are driven by multiple gut-derived antigens, we conclude that the observed defects were not specific for any single immunogen.

To determine whether the GCs in AID-Mettl3$^{fl/fl}$ mice are functional and can support B cell SHM and selective clonal expansion, we first examined the presence of antigen-specific B cells in GCs by staining cells derived from immunized mice with PE-NP$_{28}$ (which identifies total NP-specific B cells) or PE-NP$_{12}$ (which identifies NP-specific B cells that express higher-affinity B cell antigen receptors [BCRs]). Flow cytometric analysis revealed that AID-Mettl3$^{fl/fl}$ mice hosted slightly fewer NP-specific B cells in the GC, whereas the proportion of B cells that bind NP$_{12}$ was significantly reduced in these mice (Fig. 2 C). Accordingly, lower total and high-affinity NP-specific antibody titers were detected in the sera of AID-Mettl3$^{fl/fl}$ mice (Fig. 2 D). To examine if Mettl3-deficiency affects clonal expansion in the GC, individual IgG1^{+} GC B cells (responding to either NP or KLH) were sorted from single LNs followed by *Igh* mRNA sequencing. This analysis revealed that the degree of Ig diversity within the GCs of control and AID-Mettl3$^{fl/fl}$ mice was similar (Fig. 2 E). However, the typical clones that respond to NP in C57BL/6 mice (V$_H$186.2; Allen et al., 1987) were less expanded in AID-Mettl3$^{fl/fl}$ mice (33% in control compared with 11% in AID-Mettl3$^{fl/fl}$ mice; Fig. 2 E). GC B cells in AID-Mettl3$^{fl/fl}$ mice showed a small (1.3-fold) but significant reduction in the number of total mutations per cell (Fig. 2 F). Nonetheless, the ratio of replacement to silent mutations was similar, suggesting that positive selection of high-affinity variants is intact in AID-Mettl3$^{fl/fl}$ mice (Fig. 2 F). Accordingly, the few V$_H$186.2 clonal members in the Mettl3-deficient GC B cells carried a mutation in the *Igh* V$_H$186.2 gene (W33L or K59R), which serves as a marker for affinity-based selection (Allen et al., 1987; Furukawa et al., 1999).

To more thoroughly probe whether acquisition of affinity-enhancing mutations is intact in the absence of METTL3, control and AID-Mettl3$^{fl/fl}$ mice were immunized, and sorted Igλ^{+} IgG1^{+} GC B cells were subjected to *Igh* mRNA sequencing. Analysis of the V$_H$186.2 mRNA transcripts revealed normal frequencies of replacement mutations that are associated with enhanced BCR affinity in Mettl3-deficient B cells (Fig. 2 G). Accordingly, calculating the ratio between total and high-affinity NP-specific IgG in the mouse serum revealed a small decrease in average antibody affinity in AID-Mettl3$^{fl/fl}$ mice; however, the rate of high-affinity antibody formation was significantly slower compared with control mice (Fig. 2 D). Thus, affinity-based clonal selection is intact in Mettl3-deficient GC B cells, although clonal expansion of the typically selected clones is suboptimal.

Expression of dark zone (DZ)–related gene programs depends on METTL3

Our findings demonstrate that METTL3 functions are required for maintenance of GC size over time. The GC is composed of two compartments: the DZ, where B cells acquire SHM and undergo clonal expansion, and the light zone (LZ), where affinity-based selection takes place (Allen et al., 2007; Victora and Nussenzweig, 2012; Allen et al., 2004). GCs of AID-Mettl3$^{fl/fl}$ mice showed a higher proportion of LZ B cells (CXCR4^{low} CD86^{high}) compared with control mice at day 14 of the response but not at day 7 (Fig. 3 A). Immunohistochemical analysis of the topographical localization of GC B cells within the DZ and LZ in chimeric mice confirmed the decrease in Mettl3-deficient cells at day 14. Furthermore, the number of Mettl3-deficient B cells in the DZ was reduced compared with the control, whereas no change was observed in the LZ. This finding suggests that LZ-to-DZ trafficking is not compromised in the absence of METTL3 (Fig. S3 A). To determine which molecular mechanisms depend on METTL3 functions in specific GC sites, LZ and DZ B cells were sorted from control and AID-Mettl3$^{fl/fl}$ mice and subjected to RNA-seq 7 and 14 d after immunization. Analysis of differential gene expression revealed that METTL3 plays a significant role in regulating gene expression in the DZ, while very small reproducible transcriptional differences were observed in the LZ at both time points (Figs. 3 B and S3 B). Some transcriptional heterogeneity was found within the LZ in individual mice, but was not reproduced across several mice, as shown by principal component analysis (Fig. S3 C). In Mettl3-deficient DZ B cells, 226 genes showed increased expression, whereas 100 genes showed decreased expression compared with control cells (fold-change ≥1.5, adjusted P = 0.1). Furthermore, whereas the transcriptome of control GC B cells showed expected differential gene expression between LZ and DZ, Mettl3-deficient GC

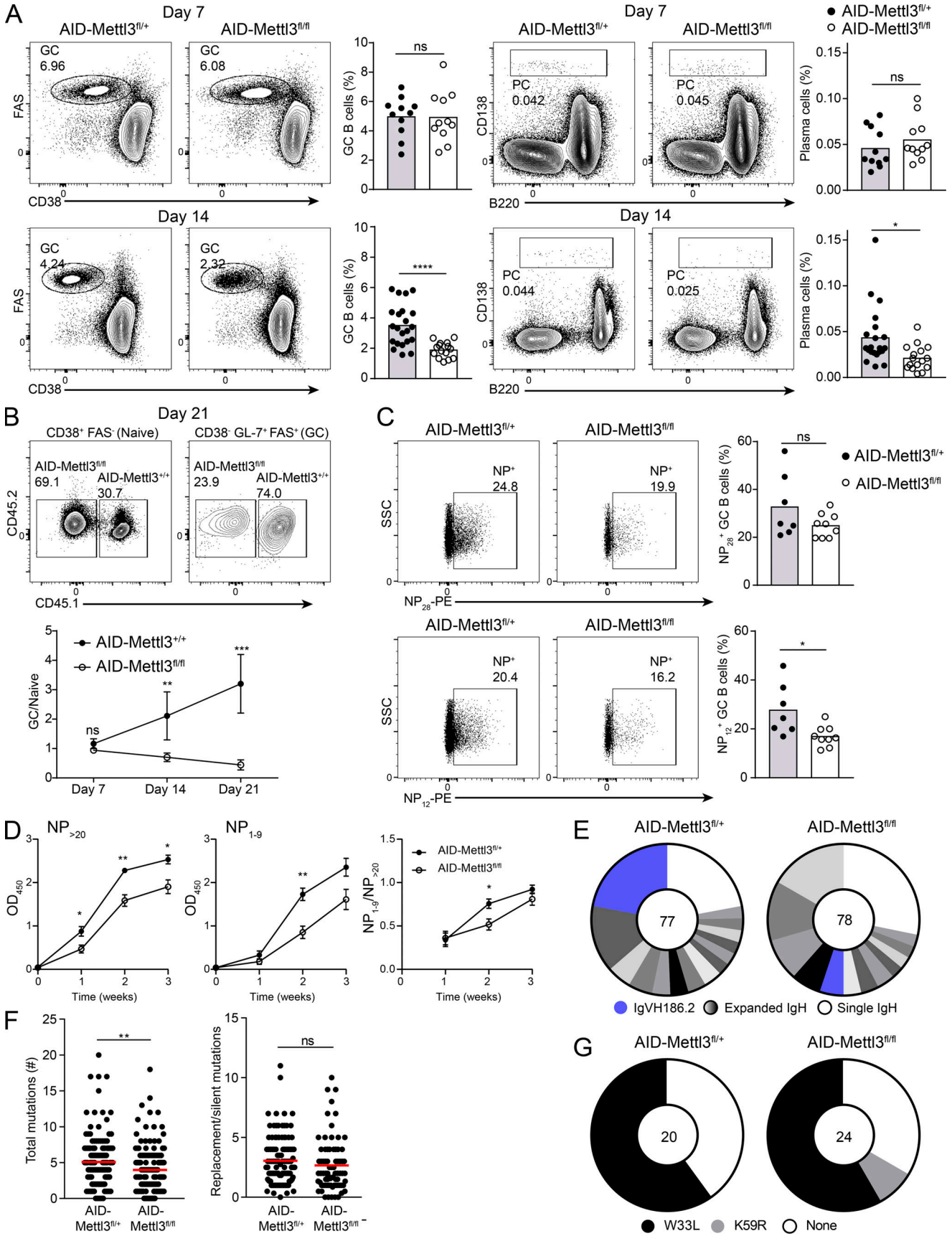

Figure 2. **METTL3 is required for durable GC reactions and proper clonal expansion. (A)** The frequency of GC B cells and PCs in control and AID-Mettl3$^{fl/fl}$ mice 7 and 14 d after NP-KLH immunization. Data are pooled from four to seven independent experiments with a total of 11–22 mice per group. Each data point

represents a single mouse, and column heights represent mean values. SSC, side scatter. **(B)** Chimeric mice were generated by transfer of a mixture of cells containing 30% control BM cells ($AID^{cre/+}$) and 70% AID-$Mettl3^{fl/fl}$ BM cells. 1–3 wk after immunization with NP-KLH, the proportion of control ($CD45.1^+$) and Mettl3-deficient ($CD45.2^+$) cells in the naive and GC compartments in popliteal LNs was analyzed by flow cytometry. Data are pooled from two to three experiments, with two to three mice per condition. Mean ± SD are indicated. **(C)** The proportion of GC B cells that bind NP28-PE (total antigen-specific B cells) and cells that bind NP12-PE (high-affinity antigen-specific B cells) 21 d after immunization. Each data point represents a single mouse, and columns represent mean values. Pooled data from three experiments with a total of seven to nine mice per group. **(D)** ELISA of total and high-affinity NP-specific antibodies in AID-$Mettl3^{fl/fl}$ and control mice. Dots represent the mean of seven to nine mice with SEM. **(E and F)** Single-cell analysis of immunoglobulin diversity (E), SHM frequency, and amino acid replacement ratio (F) in $IgG1^+$ GC B cells derived from control and AID-$Mettl3^{fl/fl}$ mice 21 d after NP-KLH immunization. Each slice in D represents a cluster of sequences with identical combinations of VDJ sequences. Each data point in E represents a single Ig gene, and lines represent mean values. **(G)** Frequencies of W33L and K59R mutations in VH186.2 of GC B cells as measured by bulk *Igh* sequencing. Each slice represents a cluster of sequences with the indicated mutations. Two experiments each with one mouse per condition were performed and are shown in a representative plot (D) or as pooled data (E and F). Two-tailed Student's *t* test (A, C, and D) or one-way ANOVA corrected for multiple comparisons (Sidak; B) was used for statistical analysis. *, $P < 0.05$; **, $P < 0.01$; ***, $P < 0.005$; ****, $P < 0.001$.

B cells showed very small transcriptional differences between these compartments (Fig. 3 C). Consistently, gene set enrichment analysis (GSEA; Subramanian et al., 2005) revealed that Mettl3-deficient DZ B cells (sorted as $CXCR4^{high}$ and $CD86^{low}$) did not express typical DZ genes, but rather showed increased expression of the typical LZ transcriptional program (Fig. 3 D). Although the mRNA level of *Cxcr4* was decreased in Mettl3-deficient cells, no significant changes were observed at the protein level, suggesting additional mechanisms that specifically compensate for the transcriptional impairment (Fig. S3 D). Transcription of genes that regulate critical biological processes in the DZ, including cell cycle, DNA repair, and RNA metabolic pathways, were significantly reduced in Mettl3-deficient DZ B cells (Fig. 3 E). In addition, GSEA revealed that cell cycle–, oxidative phosphorylation–, and DNA repair–related genes were down-regulated, whereas genes that are part of the apoptosis pathway were up-regulated, compared with control mice (Fig. 3, F and G). Furthermore, the MYC signature, which is associated with proper GC functions and positive B cell selection, was down-regulated. Accordingly, gene expression signatures that are associated with B cell selection and GC core genes were not properly expressed (Fig. 3, F and G). Together, these results indicate that although discernible DZ and LZ compartments expressing zone-specific markers are formed independently of METTL3, this enzyme is required for proper expression of typical DZ-associated gene programs, including genes that are activated by MYC and cell cycle–related genes.

METTL3 expression by GC B cells is required for efficient cell cycle progression

To verify our transcriptomic findings in functional assays, we sought to measure cell division and cell cycle stages in GC B cells. To this end, we pulsed immunized mice with 5-ethynyl-2′-deoxyuridine (EdU) by i.v. injection and examined the frequency of EdU^+ cells after 2.5 h. Flow cytometric analysis revealed that Mettl3-deficient GC B cells proliferated to a lesser degree than cells derived from control mice during this short experimental period (~5% fewer Mettl3-deficient GC B cells per 2.5 h, 17% fewer compared with controls; Fig. 4 A). Co-labeling of DNA-incorporated EdU and total DNA revealed that significantly fewer cells were detected in the S-phase of the cell cycle in Mettl3-deficient GC B cells (Fig. 4 B), and similar defects were detected in LZ and DZ compartments (Fig. S3 E). These small differences in cell cycle progression reflect a defect in proliferation capacity that can greatly affect the number of GC B cells over time.

The transcriptomic analysis revealed that genes involved in apoptosis are up-regulated in Mettl3-deficient GC B cells. To determine if the reduction in GC B cell frequencies is also a result of an increase in apoptotic events, in addition to reduced proliferation, we examined the activity of caspase-3/7. To distinguish between apoptotic and dead cells, we colabeled B cells with a DNA dye (SYTOX AADvanced [SAAD]) and a cleavable peptide that labels cells with active caspase-3/7. SAAD- and active caspase-3/7–positive signals label dead cells, whereas SAAD-negative and active caspase-3/7–positive signals label apoptotic cells. As expected, very few apoptotic cells were observed in the naive B cell compartment (Fig. 4 C). In contrast, apoptotic cells were clearly detected in the GC cell population, and their frequency in Mettl3-deficient GC B cells was threefold higher than in the control cells in both DZ and LZ (Fig. 4 C). Consistent with the lack of effect on GC size on day 7 after immunization, Mettl3-deficient B cells did not show significantly increased apoptosis at this time point, although a trend in that direction was observed (Fig. 4 D). These results demonstrate that METTL3 activity prevents excess B cell apoptosis in the GC reaction.

AID enzymatic activity inserts mutations into the *Igh* genes that may result in the inability of GC B cells to express a functional BCR (Mayer et al., 2017; Stewart et al., 2018). In addition, this enzyme acts as a major driver of off-target DNA damage events and chromosomal translocations in GC B cells (Casellas et al., 2016). Furthermore, AID activity induces DNA double-strand breaks, and METTL3 was suggested to play a role in the subsequent DNA repair mechanisms (Zhang et al., 2020; Daniel and Nussenzweig, 2013). To examine whether enhanced apoptosis and reduction in the frequency of GC B cells is a result of AID-mediated DNA damage or defects in the subsequent DNA repair mechanism, we generated $Aicda^{cre/cre}$ $Mettl3^{fl/+}$ and $Aicda^{cre/cre}$ $Mettl3^{fl/fl}$ mice that lack expression of the AID enzyme. The deletion of AID did not increase the frequency of GC B cells in $Aicda^{cre/cre}$ $Mettl3^{fl/fl}$ immunized mice to approach that of the control mice on day 14 after immunization, and the DZ-to-LZ ratio defect remained (Fig. 4 E). These results indicate that deficiency in neither AID functions nor DNA repair of AID-mediated DNA damage can account for the decreased GC cell number in Mettl3-deficient mice. Furthermore, BCR downstream signaling was intact in Mettl-deficient

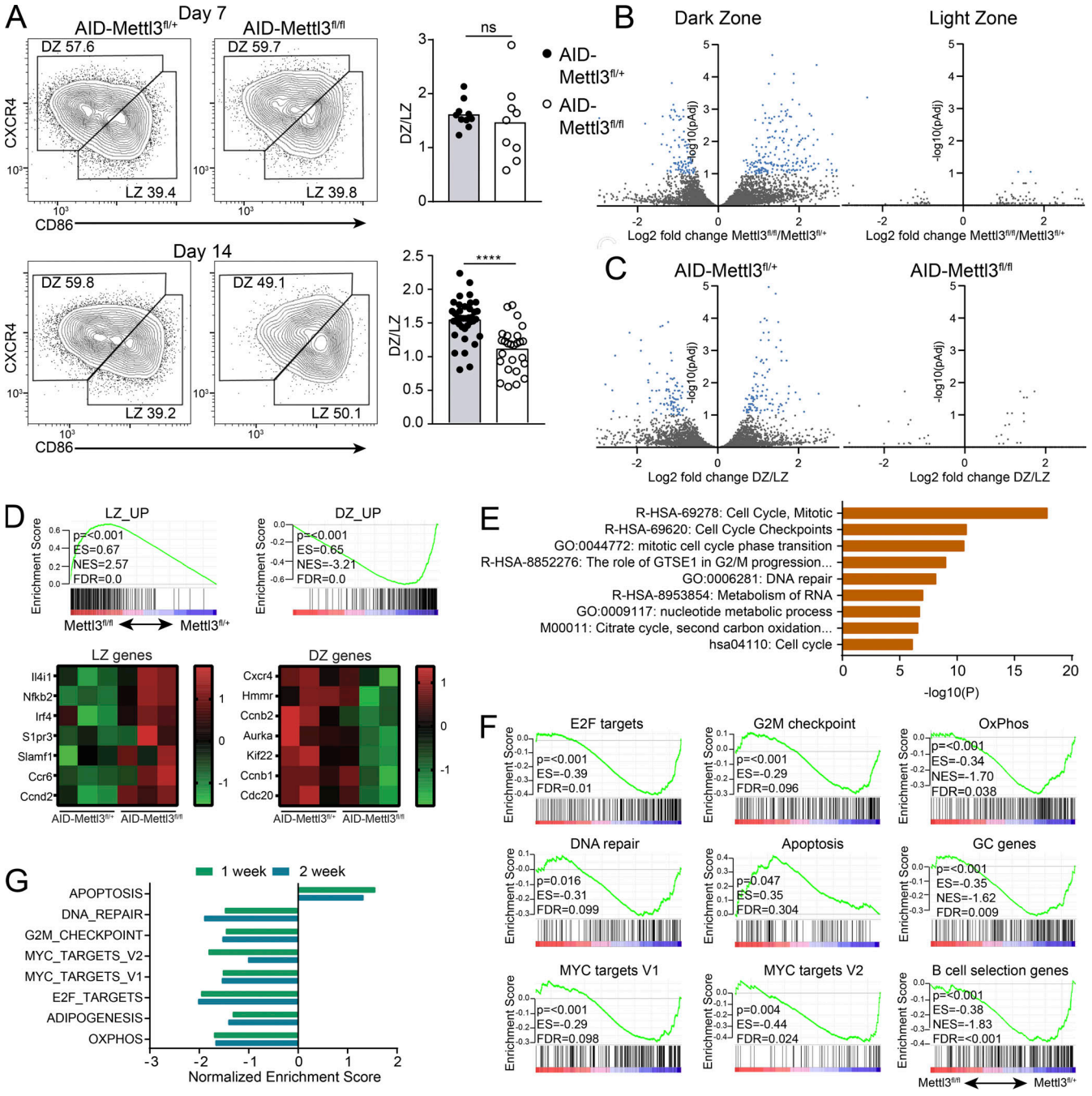

Figure 3. **METTL3 modulates cell cycle–related genes in the GC DZ. (A)** The distribution of GC B cells to DZ and LZ subsets in control and AID-Mettl3$^{fl/fl}$ mice 7 and 14 d after NP-KLH immunization. Data pooled from four to seven experiments with a total of 11–22 mice per group. Each data point represents a single mouse, and column heights represent mean values. **(B)** Differential gene expression in LZ and DZ GC B cells derived from mice in A (three mice per condition), 14 d after immunization. **(C)** Differential gene expression between LZ and DZ GC B cells in either control or AID-Mettl3$^{fl/fl}$ mice. **(D)** GSEA and heatmap representation of DZ- and LZ-related gene expression 14 d after immunization. ES, enrichment score; FDR, false discovery rate; NES, normalized enrichment score. **(E)** Gene annotation analysis was performed on down-regulated genes in Mettl3-deficient DZ B cells (fold-change ≥1.5, adjusted P = 0.1) 14 d after immunization, using Metascape online tool. **(F)** GSEA analysis of DZ GC B cells 7 d after immunization. **(G)** Normalized gene enrichment scores for gene sets shown in F 7 and 14 d after immunization. OXPHOS, oxidative phosphorylation. Two-tailed unpaired Student's *t* test. ****, P < 0.001.

GC B cells, suggesting that these cells can effectively respond to antigens in the GC (Fig. S3 F). Collectively, these results suggest that METTL3 supports B cell persistence and attenuates apoptosis in the GC, primarily through regulation of proliferation.

METTL3 regulates different gene programs in GCs through the functions of distinct m^{6}A readers

IGF2BPs are a family of mRNA-binding proteins that increase the mRNA lifetime of target genes and whose binding capacities are enhanced by m^{6}A methylation (Palanichamy et al., 2016; Ren

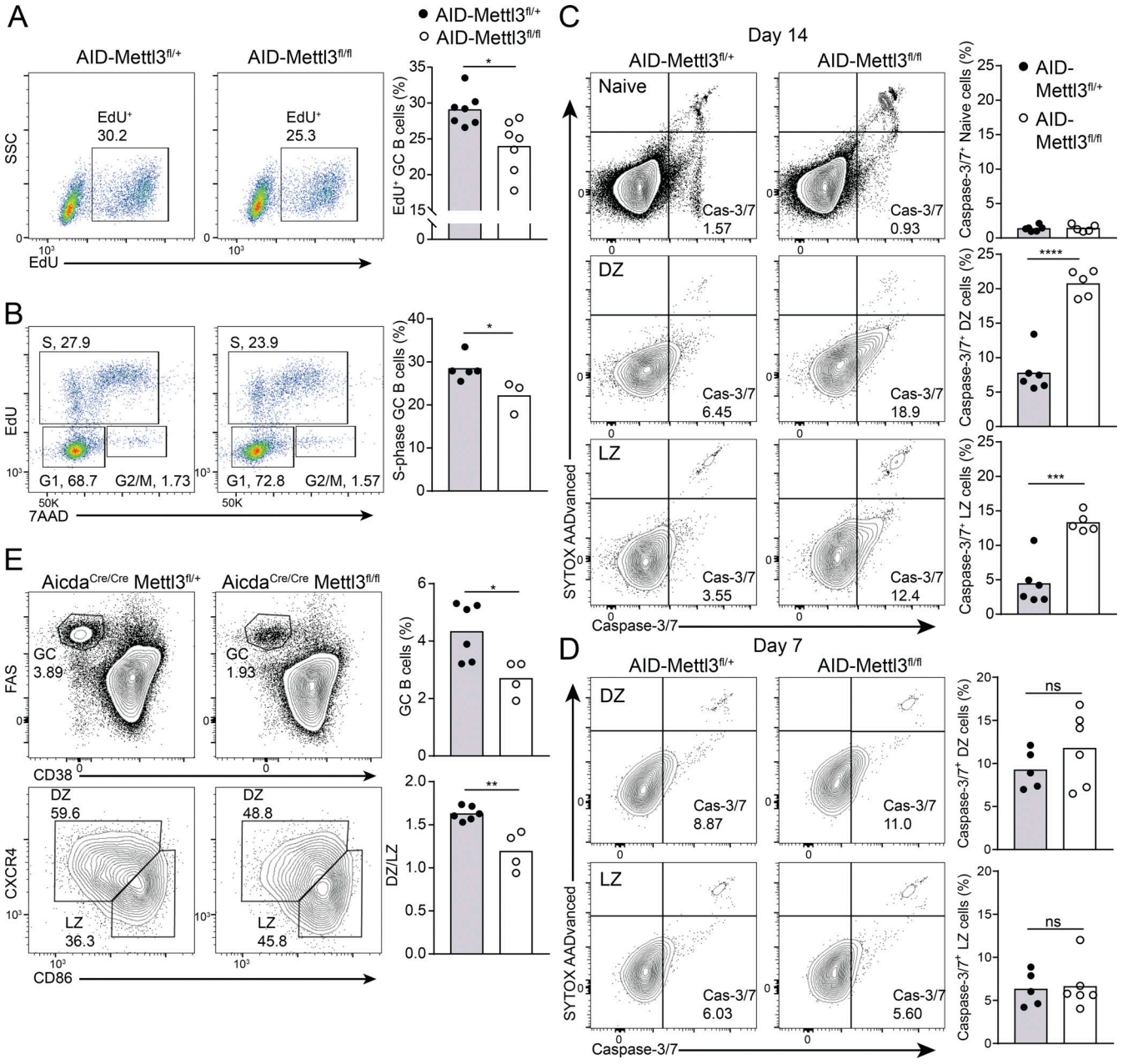

Figure 4. **Effective cell cycle progression of GC B cells depends on METTL3. (A and B)** Analysis of the different cell cycle stages in GC B cells by EdU incorporation and 7AAD DNA staining 14 d after NP-KLH immunization. Data are pooled from two to three experiments with a total of seven mice per group. SSC, side scatter. **(C and D)** The frequency of apoptotic cells measured by a caspase-3/7 activity assay and DNA content in naive, DZ, and LZ B cells 14 (C) and 7 (D) d after immunization. Data are pooled from two independent experiments with a total of five to six mice per group. **(E)** GC formation in Aicda$^{Cre/Cre}$ Mettl3$^{fl/+}$ and Aicda$^{Cre/Cre}$ Mettl3$^{fl/fl}$ mice 14 d after immunization. Each data point represents a single mouse, and column heights represent mean values. Data are pooled from two independent experiments with a total of four to six mice per group. Two-tailed Student's *t* test was used to determine statistical significance. *, P < 0.05; **, P < 0.01; ***, P < 0.005; ****, P < 0.001.

et al., 2020; Huang et al., 2018; Samuels et al., 2020). IGF2BP2 plays a role in regulation of mRNAs in Th17 cells through interaction with m^{6}A (Bechara et al., 2021). IGF2BP3 binds the 3′-UTR of *Myc* mRNA and is the main paralog expressed in immune cells (Palanichamy et al., 2016). Because we found that the Myc pathway is down-regulated in Mettl3-deficient GC B cells, and because m^{6}A enhances IGF2BP3 regulation of *Myc* mRNA (Huang et al., 2018), we sought to examine the role of IGF2BP3 in GCs. The size of the GC compartment 7 d after immunization in Igf2bp3-deficient mice was similar to that of WT mice; however, the frequency of GC B cells decreased after an additional 7 d (Figs. 5 A and S4 A). This defect was B cell specific, as a similar phenotype was observed in chimeric mice hosting both WT and Igf2bp3$^{-/-}$ immune cells (Fig. S4 B). In addition, Igf2bp3-deficient B cells responded to anti-IgM stimulation in vitro, suggesting that this mRNA binder does not play a role in B cell activation (Fig. S1 I). To examine the effect of IGF2BP3 on MYC-responsive genes, GC B cells were isolated from mice 14 d after

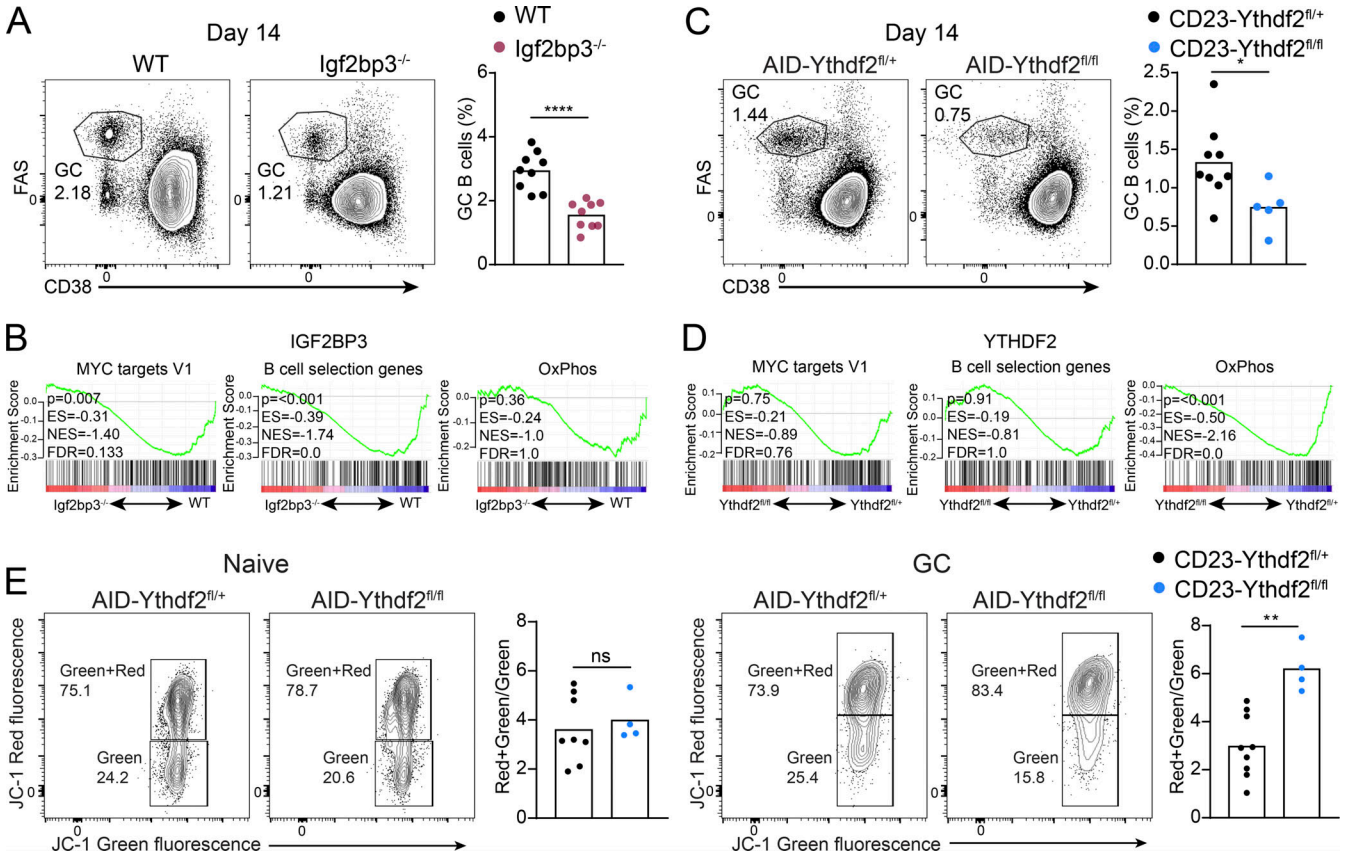

Figure 5. **IGF2BP3 regulates MYC-target gene expression, whereas YTHDF2 controls oxidative phosphorylation gene programs and mitochondrial functions. (A)** The frequency of GC B cells in WT and Igf2bp3$^{-/-}$ mice 14 d after NP-KLH immunization. Data pooled from three experiments with a total of nine mice per group. **(B)** GSEA of MYC targets, GC B cell selection–related and oxidative phosphorylation–related genes in WT and Igf2bp3-deficient GC B cells. Gene expression differences based on three to four mice per condition. **(C)** The frequency of GC B cells in CD23-Ythdf2$^{fl/+}$ and CD23-Ythdf2$^{fl/fl}$ mice 14 d after NP-KLH immunization. Data pooled from two experiments with a total of five to nine mice per group. **(D)** GSEA as in B in GC B cells derived from AID-Ythdf2$^{fl/+}$ and AID-Ythdf2$^{fl/fl}$ mice. Gene expression differences based on two mice per condition. **(E)** JC-1 staining of naive and GC B cells in AID-Ythdf2$^{fl/+}$ and AID-Ythdf2$^{fl/fl}$ mice. Green signal represents the mitochondrial mass, and red signal shows mitochondrial membrane charge. The quantification shows the ratio of these measurements. Each data point represents a single mouse, and column heights represent mean values. Data pooled from two independent experiments with a total of four to eight mice per group. Two-tailed Student's *t* test. *, P < 0.05; **, P < 0.01; ****, P < 0.001.

immunization and subjected to RNA-seq followed by GSEA. Significant down-regulation of MYC-responsive genes, GC-related genes, and B cell selection signatures, as well as a loss of the DZ transcriptional program, were observed in Igf2bp3-deficient mice (Fig. 5 B and Fig. S4, C and D). In contrast to the changes in gene signature observed in Mettl3-deficient B cells, we did not detect reduction in expression of genes that are associated with oxidative phosphorylation (Fig. 5 B). Collectively, we conclude that IGF2BP3 is required for adequate expression of MYC-downstream targets in GC B cells.

YTHDFs are a family of mRNA binders that interact with m^{6}A, and the YTHDF2 paralog is associated with transcript destabilization and degradation (Du et al., 2016; Wang et al., 2014; Zaccara and Jaffrey, 2020). YTHDF2 is the dominant paralog in GC B cells (Fig. S4 E). To examine whether the inability of YTHDF2 to bind m^{6}A in Mettl3-deficient mice also accounts for defects in B cell functions, we produced CD23-Cre Ythdf2$^{fl/fl}$ and AID-Cre Ythdf2$^{fl/fl}$ (CD23- and AID-Ythdf2$^{fl/fl}$) mouse strains (Ivanova et al., 2017). Specifically, the CD23-Ythdf2$^{fl/fl}$ strain was used for GC size analyses, and to avoid pre-GC defects, the AID-Ythdf2$^{fl/fl}$ strain was used for gene expression and subsequent functional analyses. In CD23-Ythdf2$^{fl/fl}$ mice, GCs were detectable in response to immunization; however, they were smaller compared with their control counterparts in CD23-Ythdf2$^{fl/+}$ mice at day 14 after immunization (Fig. 5 C). In contrast to the results obtained in Mettl3-deficient cells, RNA-seq analyses revealed that MYC-responsive genes, the core GC genes, and gene programs associated with the selection of high-affinity clones were not altered in GC B cells derived from AID-Ythdf2$^{fl/fl}$ mice, wherein *Ythdf2* is deleted after early B cell activation (Figs. 5 D and S4 C). In contrast, GSEA analyses revealed severe down-regulation in the expression of genes that are associated with oxidative phosphorylation, which was also observed in Mettl3-deficient GC B cells (Fig. 5 D). These results suggest that YTHDF2 plays a role in the GC; however, as opposed to METTL3 and IGF2BP3, it does not enhance MYC-induced genetic programs.

Oxidative phosphorylation is the major respiratory pathway in GC B cells (Weisel et al., 2020). To examine if oxidative phosphorylation is intact in Ythdf2-deficient GC B cells, we used a probe (JC-1) that allows assessment of mitochondrial health by

measuring the polarization of this organelle. Ythdf2-deficient GC cells stained with the JC-1 probe exhibited hyperpolarized mitochondria compared with control GC cells, which suggests a defect in the mitochondrial electron transport chain (Fig. 5 E). This defect was not observed in naive B cells in which Ythdf2 is not deleted. In contrast, analysis of metabolism in naive and activated B cells in vitro using the Seahorse system did not reveal a pronounced defect in either oxidative phosphorylation or glycolysis, suggesting that either the observed defects are specific for GC B cells in situ or that the metabolic status in cultured B cells is different from GC B cells under physiological conditions (Fig. S4 F). Collectively, we conclude that intact proliferation through MYC expression as well as mitochondrial functions depend on the m^{6}A machinery in GC B cells.

Adequate *Myc* mRNA levels in GC B cells depend on METTL3 and IGF2BP3

The GC reaction and selection of high-affinity clones by T cells depend on MYC functions and activation of downstream gene transcription promoting clonal expansion (Calado et al., 2012; Dominguez-Sola et al., 2012). Therefore, we examined in depth how *Myc* expression is regulated by the m^{6}A machinery. RT-qPCR analysis of sorted GC B cells revealed reduced levels of *Myc* mRNA in Mettl3-deficient LZ B cells, and lower expression of MYC protein was observed in LZ B cells derived from AID-Mettl3$^{fl/fl}$ mice that express MYC-GFP compared with AID-Mettl3$^{fl/+}$ littermates (Fig. 6, A and B; Huang et al., 2008). We also examined Myc expression in this model at early time points using PE-specific cells and RT-qPCR. Here, we did not find a significant reduction in *Myc* expression, consistent with the observation that GC formation at day 7 was intact in this model (Fig. S4 G). However, lower levels of MYC protein were also observed in PE-specific B cells derived from CD23-Mettl3$^{fl/fl}$ mice 3 d after immunization with PE, suggesting that METTL3 regulates Myc early during the response as well (Fig. S4 H). Consistent with the decrease in Myc levels in Mettl3-deficient GC B cells, Igf2bp3-deficient GC B cells showed reduced *Myc* mRNA and protein levels; in contrast, Ythdf2-deficient cells did not show a reduction in *Myc* mRNA levels (Fig. 6, C–E). These findings indicate that METTL3 maintains sufficient *Myc* mRNA and protein through IGF2BP3 functions rather than YTHDF2. To examine whether the defect in maintenance of sufficient *Myc* transcripts through METTL3 activity is the reason for the reduction in the frequency of GC B cells in AID-Mettl3$^{fl/fl}$ mice, we generated mice that overexpress MYC in Mettl3-deficient and -proficient GC B cells (Sander et al., 2012). AID-Mettl3$^{fl/fl}$ mice were bred with a mouse strain that carries the human *Myc* gene in the Rosa26 locus and a stop codon in front of it, flanked by *LoxP* sites (R26$^{Myc/+}$; Sander et al., 2012). Age-matched transgenic mice were immunized with NP-KLH, and GC size was examined by flow cytometry after 14 d. Whereas the frequency of GC B cells was smaller in AID-Mettl3$^{fl/fl}$ mice compared with control mice, the AID-Mettl3$^{fl/fl}$ R26$^{Myc/+}$ mice showed normal frequencies of GC cells; however, an increase in GC size was also observed in AID-Mettl3$^{fl/+}$ R26$^{Myc/+}$ mice (Fig. 6 F). Thus, METTL3 functions regulate *Myc* transcript dosage and expression of downstream genes; nonetheless, since overexpression of *Myc* also increased the frequency of GC B cells in the control mice as previously observed (Sander et al., 2012), it was impossible to determine whether suboptimal *Myc* expression is the only reason for the reduction in the frequency of GC cells over time.

Myc mRNA is methylated in GC B cells, and its stability is regulated by m^{6}A machineries

METTL3 is a methyltransferase that catalyzes the addition of m^{6}A on mRNA transcripts at consensus sites. To examine whether *Myc* mRNA carries m^{6}A modifications in B cells, we performed immunoprecipitation of methylated mRNA (m^{6}A-IP). RT-qPCR of WT in vitro–activated B cells revealed that *Myc* mRNA was highly enriched in the pull-down fraction compared with control unmethylated mRNA (*Gapdh*; Fig. 7 A). To further validate the methylation of Myc transcripts, we performed m^{6}A-IP followed by high-throughput sequencing of the input and IP fractions. To assess m^{6}A levels in control and Mettl3-deficient B cells (CD23-Mettl3$^{fl/fl}$), we compared the average IP over input fractions in both populations and in selected key B cell genes including *Myc*, and a statistically significant reduction in *Myc* mRNA methylation was detected in this assay (Fig. S5, A–F). M^{6}A-seq on mRNA derived from Mettl3-deficient B cells yielded peak over input (POI) scores that were reduced to 60% of control (Fig. S5, A–D). The m^{6}A sites that were specifically detected in control cells were enriched around m^{6}A consensus motifs, 3′-UTRs, and stop codons (Fig. S5, A–D). Notably, as previously shown, *Myc* mRNA was found to carry methylations at sites that are close to the stop-codon region in B cells (Fig. 7 B). Interestingly, AID mRNA was also methylated; however, we did not observe changes in AID mRNA transcript levels in Mettl3-deficient GC B cells (Fig. S5 G). Thus, *Myc* mRNA is methylated at typical m^{6}A sites in B cells.

To understand the magnitude of the contribution of direct m^{6}A targets to the changes in expression of gene signatures, we examined the fraction of m^{6}A targets in genes that are significantly differentially expressed in DZ GC B cells. We found 23 genes in the down-regulated fraction and 99 genes in the up-regulated fraction (Fig. S5 H). Furthermore, we analyzed the potential enrichment of m^{6}A targets in GSEA hallmark gene sets. However, we did not find any significantly enriched gene sets or single genes that could explain the observed changes in gene signatures. In addition, considering the general trend of m^{6}A target up-regulation upon deletion of Mettl3 (Fig. S5 I) and that many of the affected gene signatures were down-regulated, we conclude that, apart from Myc, many of the gene expression changes in the signatures observed in Mettl3-deficient GC B cells are due to indirect effects of m^{6}A modification.

Next, we examined how METTL3 functions regulate *Myc* transcript quantity in B cells. To gain more insight into the abundance and persistence of *Myc* mRNA in the GC at the single-cell level, we labeled *Myc* transcripts by single-molecule fluorescence in situ hybridization (smFISH; Bahar Halpern and Itzkovitz, 2016). B cells in GC structures were identified by staining with Ki-67 probes and B220 antibodies in LN slides derived from immunized mice (Fig. S5 J). Quantification of *Myc*

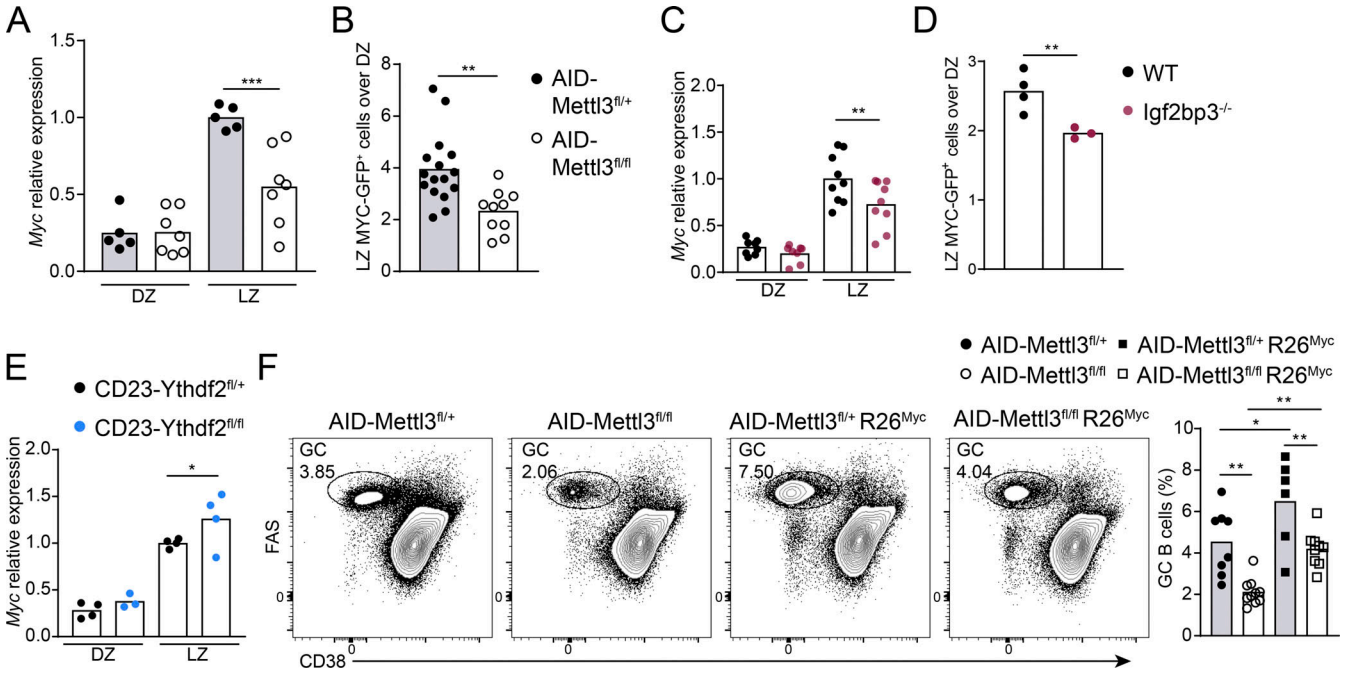

Figure 6. **METTL3 and IGF2BP3 are required for effective Myc expression. (A)** Relative *Myc* mRNA expression in GC B cells derived from AID-Mettl3$^{fl/+}$ or AID-Mettl3$^{fl/fl}$ mice 14 d after immunization. Data pooled from three independent experiments with a total of five to seven mice per group. **(B)** MYC protein expression in GC B cells derived from immunized cMYC-GFP AID-Mettl3$^{fl/+}$ and AID-Mettl3$^{fl/fl}$ mice. Relative proportions of cMYC-GFP+ cells in the GC LZ versus DZ. Pooled data from five experiments with a total of 10–16 mice per group. **(C)** Relative *Myc* mRNA expression in GC B cells derived from WT and Igf2bp3$^{-/-}$ mice 14 d after immunization. Data pooled from four experiments with a total of nine mice per group. **(D)** MYC protein expression in GC B cells derived from immunized cMYC-GFP WT and Igf2bp3$^{-/-}$ mice. Data pooled from two experiments with a total of three to four mice per group. **(E)** Relative *Myc* mRNA expression in GC B cells derived from CD23-Ythdf2$^{fl/+}$ or CD23-Ythdf2$^{fl/fl}$ mice 14 d after immunization. Pooled data from two experiments with a total of three to five mice per group. **(F)** The frequency of GC B cells was measured in age-matched AID-Mettl3$^{fl/+}$ and AID-Mettl3$^{fl/fl}$ mice with or without an R26^{Myc} allele 14 d after immunization. Pooled data from three experiments with a total of six to nine mice per group. Expression by RT-qPCR was determined relative to the housekeeping gene *Ubc*. Each data point represents a single mouse, and column heights represent mean values. Two-tailed Student's *t* test (B and D) or one-way ANOVA corrected for multiple comparisons (Holm–Sidak; A, C, E, and F). *, P < 0.05; **, P < 0.01; ***, P < 0.005.

transcript number per B cell revealed that in control mice, 1.5-fold more single GC B cells expressed ≥2 mRNA molecules compared with the corresponding Mettl3-deficient GC B cells (Fig. 7 C). The fewer Myc transcripts observed overall and in single GC B cells can be a result of ineffective transcription through modulation of upstream regulators or enhanced mRNA degradation. To distinguish between these two possibilities, we measured the transcription rate through the visualization of Myc transcription start sites (TSSs) in GC B cells by colabeling Myc exons and introns in LN sections using a previously described protocol (Bahar Halpern et al., 2015; Bahar Halpern and Itzkovitz, 2016). The transcription rate was measured based on the number of mRNA molecules in the TSS (as described in Materials and methods). Using this analysis, we found that the rate of *Myc* transcription in situ in Mettl3-deficient GC B cells was similar to that in controls (Fig. 7, D and E). By further comparing the number of *Myc* mRNA molecules per cell to the transcription rate, we calculated the rate of degradation in both control and Mettl3-deficient cells. Since we detected fewer mRNA molecules in Mettl3-deficient GC B cells while the transcription rate was intact, we found that the degradation rate was enhanced (Fig. 7, D and E; Bahar Halpern et al., 2015; Bahar Halpern and Itzkovitz, 2016). To examine if IGF2BP3 indeed stabilizes *Myc* mRNA in B cells, we measured the *Myc* mRNA decay rate by blocking transcription with actinomycin D. We found that *Myc* transcript decay is accelerated in B cells that lack IGF2BP3 (Fig. S5 K). We conclude that the lower amounts of *Myc* mRNA observed by RT-qPCR and smFISH, as well as the defect in MYC-downstream gene expression in Mettl3-deficient GC B cells, was not a result of direct or indirect defects in *Myc* transcription, but rather resulted from an enhanced *Myc* mRNA degradation rate.

Discussion

Methylation of mRNA affects various cell functions through the binding of several types of m^{6}A readers (Shulman and Stern-Ginossar, 2020; Zaccara and Jaffrey, 2020; Zaccara et al., 2019). Here, we demonstrate the role of mRNA methylation and two different mRNA binders in supporting biological processes that are critical for GC formation and maintenance. Whereas Myc expression depends on IGF2BP3, oxidative phosphorylation–related genes are modulated indirectly by YTHDF2. Together, these findings portray how distinct m^{6}A binders modulate two independent pathways that support critical processes required for effective GC functions.

MYC expression is induced rapidly upon B cell interaction with antigen, but after 2 d, the level of this protein is rapidly

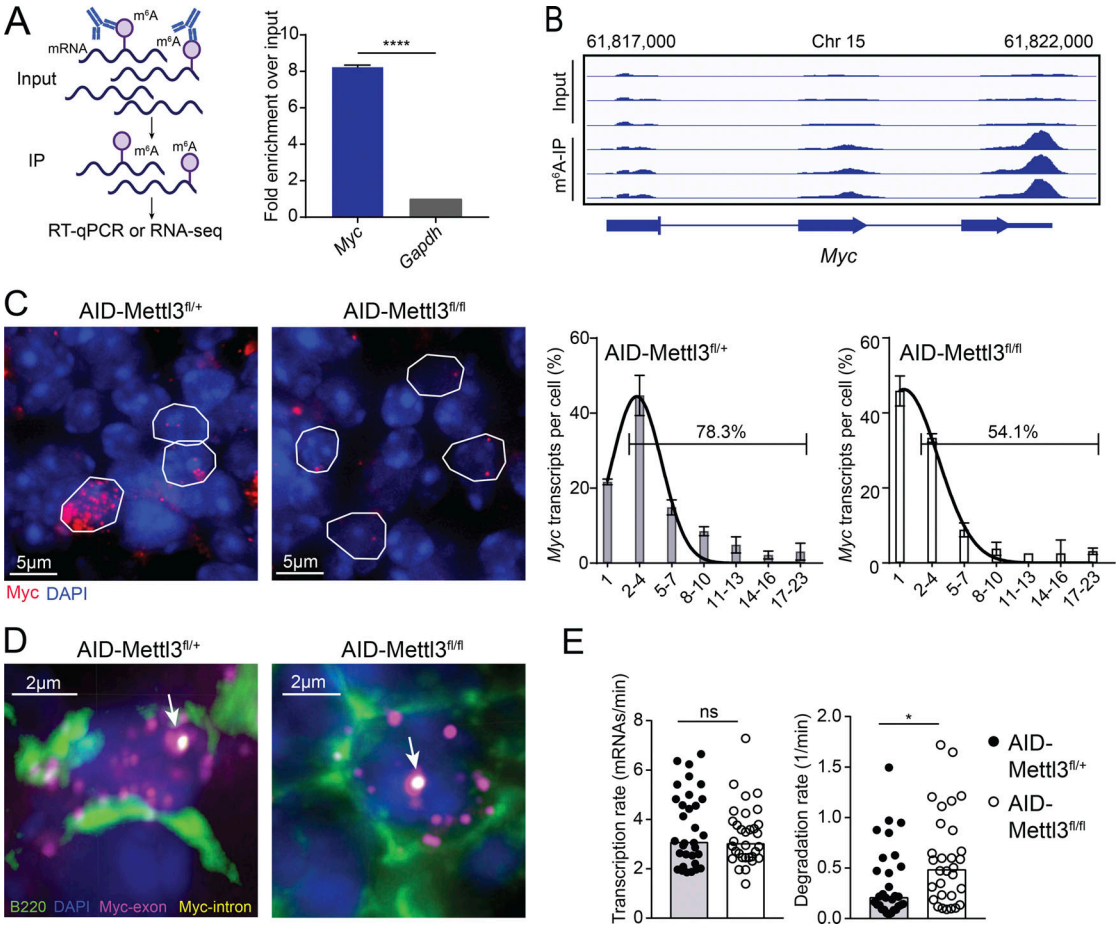

Figure 7. **METTL3-mediated mRNA methylation prolongs Myc-transcript lifetime in GC B cells. (A)** *Myc* and *Gapdh* mRNA methylation in B cells was measured by m^{6}A RNA IP followed by RT-qPCR. Fold enrichment of *Myc* mRNA in pull-down over input fraction, normalized to unmethylated *Gapdh* mRNA. Pooled data from two replicates. **(B)** *Myc* methylation site analysis by m^{6}A pull-down followed by high-throughput sequencing. Mapped reads to *Myc* from the input and m^{6}A-IP fraction are indicated. **(C and D)** *Myc* mRNA abundance in single GC B cells by smFISH. Red and magenta dots represent *Myc* mRNA detected using an smFISH probe library targeting the exons (C and D), and yellow dots represent *Myc* intronic mRNA detected using an smFISH probe library targeting the introns (D). The bar graphs in C depict the quantification of the data. GCs were identified by staining with B220 antibody and Ki-67 smFISH probe. Arrows point to dots that represent active TSS. Representative images from 2–3 mice, 3–5 GCs, and 31–35 cells per condition are shown. **(E)** *Myc* mRNA transcription and degradation rates in GC B cells as measured by smFISH in D. Column height represents the median. Unpaired Student's *t* test. *, P < 0.05; ****, P < 0.001.

decreased, followed by its limited reexpression in the fully formed GC (Dominguez-Sola et al., 2012; Calado et al., 2012). MYC expression dynamics in B cells is consistent with our findings that demonstrate a requirement for METTL3 at the early and late stages of the response, but not during initial AID expression at the time of pre-GC events (Calado et al., 2012; Dominguez-Sola et al., 2012). In particular, *Myc*-inducing factors such as cognate antigen and T cell help signals are limited at later stages of the response, when METTL3 functions and IGF2BP3 are essential for maintaining the GC reaction. Myc expression levels are important for both B cell proliferation and positive selection (Dominguez-Sola et al., 2012). The frequency of Mettl3-deficient B cells in GCs declined over time independently of competition with Mettl3-expressing cells, indicating that the m^{6}A machinery primarily plays a role in global B cell proliferation machineries in the GC, rather than specifically in the positive clonal selection process. In support of this conclusion, we found that the acquisition of SHM and affinity-enhancing mutations in the GC is METTL3 independent, whereas effective proliferation and proper expression of the GC core genes required METTL3 functions. In parallel, we found an increase in the frequency of apoptotic B cells in AID-Mettl3$^{fl/fl}$. Since GC B cells are intrinsically pro-apoptotic and depend on T cell help for effective proliferation and survival, we suggest that lack of sufficient expression of MYC-downstream genes can explain the increase in apoptosis in AID-Mettl3$^{fl/fl}$ mice. An additional explanation for the GC B cell decline may be early GC termination; however, in chimeric mice, control B cells persisted, whereas the Mettl3-deficient B cells declined over time, suggesting an intrinsic defect rather than a global one, such as reduction in antigen availability or the presence of high-affinity antibodies that block antigens in the GC (Zhang et al., 2013). Our findings are consistent with a model wherein T cells are able to distinguish between low- and high-affinity clones in the GC independently of m^{6}A modifications in B cells, while effective global and preferential clonal expansion in the GC DZ depends on m^{6}A mRNA modifications including *Myc* methylation.

The outcome of mRNA methylation depends on interactions with reader proteins. Typically, the deletion of *Mettl3* or *Ythdf2* in different cell types leads to an increase in the abundance of many target transcripts (Ivanova et al., 2017; Zaccara et al., 2019; Zaccara and Jaffrey 2020). In contrast, in vitro and in vivo analyses revealed that MYC-responsive genes are downregulated upon deletion of *Mettl3* or its binding partner *Mettl14*, primarily as a result of destabilization of *Myc* transcripts (Vu et al., 2017; Cheng et al., 2019b; Weng et al., 2018; Huang et al., 2018; Zhao et al., 2020; Cheng et al., 2019a; Barbieri et al., 2017). Indeed, m^{6}A pull-down experiments revealed that *Myc* transcripts were highly methylated in B cells. Our direct quantification of *Myc* mRNAs in GC B cells in situ demonstrates that the decline in transcript abundance is a result of transcript degradation rather than a reduction in expression of a transcription factor that controls transcript dosage. These findings are in line with several previous studies that show *Myc* destabilization in the absence of m^{6}A and introduce a physiological function for this machinery in the immune response (Cheng et al., 2019b; Vu et al., 2017; Weng et al., 2018; Ma et al., 2021).

In several nonmammalian model organisms and cell lines and in a specific subset of T cells, IGF2BP paralogs enhance the stability of several mRNAs including *Myc* transcripts, and m^{6}A has been shown to reinforce these mRNA–protein interactions (Palanichamy et al., 2016; Huang et al., 2018; Ren et al., 2020; Samuels et al., 2020; Bechara et al., 2021). Our findings add a new role to this mRNA stabilization machinery in GC B cells and demonstrate how IGF2BP3 supports cellular functions in effective establishment of antibody-mediated immunity. In contrast, maintenance of sufficient *Myc* transcript levels through METTL3 functions does not depend on the dominant YTHDF family member in GC B cells, suggesting that other pathways are controlled by this reader, including proper expression of genes that support oxidative phosphorylation (Weisel et al., 2020). YTHDF2 promotes the degradation of mRNAs, and in its absence, the levels of m^{6}A-modified mRNAs increase (Ivanova et al., 2017; Zaccara and Jaffrey, 2020). Thus, this reader most likely modulates mitochondrial respiration–related genes in an indirect manner through the regulation of upstream events. Whether YTHDF2 and IGF2BP2 depend exclusively on direct binding to m^{6}A (Huang et al., 2018) or additional indirect events, such as m^{6}A-dependent changes in mRNA conformation or direct interactions with each other, requires additional investigation (Sun et al., 2019; Youn et al., 2018; Weidensdorfer et al., 2009; Zaccara et al., 2019). Expression of oxidative phosphorylation–associated genes is also regulated by HuR, an additional RNA binder that plays a role in B cell functions (Diaz-Muñoz et al., 2015). The interplay between HuR functions and YTHDF paralogs requires further investigation.

Collectively, our findings describe how the m^{6}A machinery supports central processes in the adaptive immune response through distinct m^{6}A readers. The study suggests that components of the m^{6}A machinery may serve as targets for manipulation of the adaptive arm of the immune system in MYC-driven lymphoma. In addition, since GC cells depend on mitochondrial respiration for energy generation, drugs that target the m^{6}A machinery are expected to interfere with the GC reaction and can potentially alleviate symptoms in antibody-driven autoimmunity.

Materials and methods

Mice

Mettl3$^{fl/fl}$ mice were provided by J.H. Hanna and crossed to Cre-expressing mice; B cell–specific Cd23cre mice were generated and provided by M. Busslinger (Research Institute of Molecular Pathology, Vienna, Austria). Aicda$^{Cre/+}$, Cd19-Cre, R26$^{flox\text{-}stop\text{-}flox\ Myc}$, MYC-GFP, and Igf2bp3$^{-/-}$ mice were purchased from The Jackson Laboratory. Ythdf2$^{fl/fl}$ were provided by Donal O'Carroll (University of Edinburgh, Edinburgh, UK). MYC-GFP–expressing mice were bred to mice carrying Aicda^{Cre} and Mettl3$^{fl/fl}$ alleles. WT mice (C57BL/6) were purchased from Envigo. WT and transgenic mice were used at the age of 6–12 wk. To avoid age variations in experiments that included a small number of mice carrying the R26$^{flox\text{-}stop\text{-}flox\ Myc}$ gene, only age-matched mice (~8 wk) were used. All experiments on mice were approved by the Weizmann Institute Animal Care and Use Committee.

Chimeric mice

Chimeric mice were generated by irradiating host mice with 950 rad followed by injection of fresh BM cells. For the generation of mixed chimeras, CD45.2$^+$ hosts were reconstituted with a mixture of BM cells derived from Aicda$^{Cre/+}$ CD45.1$^+$ (30%) and Aicda$^{Cre/+}$ Mettl3$^{fl/fl}$ CD45.2$^+$ (70%) mice or from CD45.1$^+$ (50%) and Igf2bp3$^{-/-}$ CD45.2$^+$ (50%) mice. Experiments with chimeric mice were performed 8 wk after BM transplantation.

Immunizations

NP-KLH (BioSearch Technologies) was prepared with alum and PBS at a final concentration of 0.4 mg/ml. Mice received a single administration to each footpad of 25 µl (10 µg NP-KLH). For immunizations with PE, 10 µg PE (Molecular Probes) in alum was injected.

In vivo EdU proliferation and apoptosis measurements

Immunized mice were injected i.v. with 2 mg of the nucleoside analogue EdU (Molecular Probes) in PBS. After 2.5 h, popliteal LNs were dissected, and isolated LN cells were stained for surface antigens as described below, followed by EdU detection using the Click-iT EdU Alexa Fluor 647 Flow Cytometry Assay Kit (Molecular Probes) according to the manufacturer's instructions. 7AAD was from BD Biosciences and added according to the manufacturer's instructions.

For measurements of apoptosis and cell death, popliteal LNs from immunized mice were isolated, and single-cell suspensions were stained for GC surface antigens and analyzed for apoptotic events using CellEvent Caspase-3/7 Green Flow Cytometry Assay Kit (Molecular Cell Probes) according to the manufacturer's instructions.

Flow cytometry

Popliteal LNs were removed, washed in cold PBS, and forced through a mesh into PBS containing 2% FCS and 1 mM EDTA to create single-cell suspensions. Cell suspensions from PPs were

similarly prepared by excising PPs from small intestines pre-washed with ice-cold PBS to remove fecal content. To block Fc receptors, washed cells were incubated with 2 µg/ml anti-16/32 (TruStain FcX, BioLegend) for 5–10 min before antibody staining. Cells were subsequently incubated with fluorescently labeled antibodies (Table S1) for 30 min on ice. Intracellular antibody staining was performed after fixation and permeabilization with Fixation/Permeabilization Solution Kit (BD Biosciences).

GC cells were gated as live/single, $B220^+$ $CD38^-$ FAS^+, and/or $GL\text{-}7^+$. DZ and LZ cells were gated as $CXCR4^{hi}$ $CD86^{lo}$ and $CXCR4^{lo}$ $CD86^{hi}$. BM transplanted cells in chimeric mice were distinguished by staining cell suspensions with GC markers, as indicated, in addition to the congenic markers CD45.1 and CD45.2 (eBioscience and BioLegend, respectively). Antigen-specific cells in PE- and NP-KLH immunization experiments were detected by staining cell suspensions with GC markers along with PE, PE-NP12, or PE-NP28. Stained cell suspensions were analyzed using a CytoFlex flow cytometer (Beckman Coulter). For RNA-seq, cells were stained for negative markers (dump$^-$: $CD4^-$, $CD8^-$, GR-1^-, and $F4/80^-$) in addition to GC markers, sorted directly into 40 µl Lysis/Binding buffer (Life Technologies) using a FACS ARIA II or FACS ARIA III (BD) instrument, and immediately frozen on dry ice.

For analysis of mitochondrial mass and membrane potential, single-cell LN suspensions were first stained with surface antibodies. Cells were then incubated with 0.3 µg/ml JC-1 probe (Invitrogen) or 50 nM Mitoview-Green probe (Biotium) at 37°C for 30 min and washed in 2 ml PBS before analysis by flow cytometry.

In vitro proliferation assay

Splenic cells from CD23-$Mettl3^{fl/fl}$ and control mice or $UBC^{CreERT2}$-$Mettl3^{fl/fl}$ mice were stained with CellTrace Violet (Invitrogen) according to manufacturer's instructions and seeded at 1×10^6 cell density in a 96-well plate. Cells were stimulated with 0–10 µg/ml LPS or anti-IgM for 3 d in a 37°C cell incubator, and CellTrace Violet dilution was assessed by flow cytometry. Half of the cells from $UBC^{CreERT2}$-$Mettl3^{fl/fl}$ mice were treated with 1 µM 4OHT for 24 h and washed in fresh RPMI before stimulation.

ERK phosphorylation assay

Phosphorylation of ERK upon BCR engagement was analyzed by stimulating isolated (using anti-CD43 negative-selection beads, Miltenyi) splenic B cells with anti-IgM for 0–30-min time intervals. 200 µl of 1×10^6 B cell suspension was added to Eppendorf tubes; 0.4 mM H_2O_2, together with 10 µg/ml anti-IgM, was added and the sample tube was vortexed. Samples were incubated in a 37°C cell incubator for indicated time intervals (see figure legends). Cells were fixed by adding 150 µl 4% paraformaldehyde and incubating for 15 min at room temperature. All samples in an independent experiment were processed together by washing with PBS and then permeabilizing and preserving the cells with 200 µl ice-cold methanol. Permeabilized cells were incubated for a minimum of 45 min on ice or kept overnight at −80°C and then washed twice with FACS buffer (see Flow cytometry) before pERK staining. Flow cytometry was used to determine the levels of pERK staining.

Transcriptomic analysis

mRNA from 2–5 × 10^4 sorted cells was captured with 12 µl of oligo(dT) Dynabeads (Life Technologies), washed, and eluted at 85°C with 6.5 ml of 10 mM Tris-HCl (pH 7.5). A bulk adaptation of the massively parallel single-cell RNA sequencing protocol (MARS-seq; Jaitin et al., 2014; Keren-Shaul et al., 2019) was used to generate RNA-seq libraries for expression profiling of GC B cells from AID-$Mettl3^{fl/+}$ and AID-$Mettl3^{fl/fl}$ mice 1 and 2 wk after immunization, AID-Ythdf2fl/+ and AID-Ythdf2fl/fl mice 1 wk after immunization, or WT and $Igf2bp3^{-/-}$ mice 2 wk after immunization. Two to four biological replicates were included in each population. Briefly, mRNA from each sample was barcoded during RT and pooled. Following Agencourt Ampure XP bead cleanup (Beckman Coulter), the pooled samples underwent second-strand synthesis and were linearly amplified by T7 in vitro transcription. The resulting RNA was fragmented and converted into a sequencing-ready library by tagging the samples with Illumina sequences during ligation, RT, and PCR. Libraries were quantified by Qubit and TapeStation as well as by qPCR for the ACTB gene as previously described (Jaitin et al., 2014; Keren-Shaul et al., 2019). Sequencing was done using a Nextseq 75-cycle high-output kit (Illumina; paired-end sequencing). Sequencing data have been deposited into the NCBI Gene Expression Omnibus under accession no. GSE180359.

Alignment and differential expression analyses were performed using the UTAP pipeline (Kohen et al., 2019). Reads were trimmed using Cutadapt and mapped to the *Mus musculus* genome (UCSC mm10) using STAR (Dobin et al., 2013) v2.4.2a with default parameters. The pipeline quantifies the genes annotated in RefSeq (extended by 1,000 bases toward the 5′ edge and 100 bases in the 3′ direction). Counting of sequenced reads was done using htseq-count (Anders et al., 2015; union mode). Genes having a minimum of five unique molecular identifier–corrected reads in at least one sample were included in the analysis. Normalization of the counts and differential expression analysis was performed using DESeq2 (Love, Huber, and Anders 2014) with the following parameters: betaPrior = true, cooksCutoff = false, and independentFiltering = false. Raw P values were adjusted for multiple testing using the procedure of Benjamini and Hochberg.

Gene annotation and pathway analysis was performed using Metascape (Zhou et al., 2019). GSEA was performed using GSEA 3.0 with the GSEA-preranked tool (Mootha et al., 2003; Subramanian et al., 2005). Gene names were converted to human gene symbols, and GSEA was run with default parameters (1,000 permutations). The Molecular Signature Database hallmark gene sets were used to perform pathway enrichment analysis using a hypergeometric distribution. Gene sets for GC formation and GC B cell selection were generated from GSE110669 and GSE98778, respectively, based on the 200 most significantly up-regulated genes in each condition. The dataset used for expression profiling in GC and DZ and LZ cells was GSE93554.

RT-qPCR

RNA was extracted using Dynabeads mRNA DIRECT Purification Kit (Invitrogen) and converted to cDNA using either qScript (Quantabio) or Super Script III (Invitrogen) enzyme according to the manufacturer's instructions with a mix of random and poly

A–specific primers. For RT-qPCR reactions, a QuantStudio 5 Real-Time PCR system and Fast SYBR Green Master Mix (Applied Biosystems) were used. Primers are listed in Table S2. Stability assays were performed by incubating isolated B cells with 5 µg/ml actinomycin D in RPMI complete medium for 0–40-min intervals before lysis and RNA extraction.

ELISA for total Ig titers

Serum was collected from multiple mice in several experiments, and titers of IgM, IgG1, and IgG2 antibodies were determined by a single direct ELISA. Diluted serum was used to coat 96-well plates by incubating overnight at 4°C. Relative quantities of antibodies were detected using HRP-conjugated anti-mouse IgM, IgG1, and IgG2 (Abcam) conjugated to HRP. NP-specific ELISAs were performed by first incubating ELISA plates with 5 µg/ml NP1-9 or NP>20 BSA overnight at 4°C. Diluted serum was incubated for 2 h at room temperature before detection.

Immunohistochemistry

Fixed single popliteal LNs were frozen in optimum cutting temperature compound and cut into 7-µm sections. Slides were blocked and incubated with fluorescently labeled antibodies. B220-PE, Streptavidin-647, IgD-PE, and GL-7-A647 antibodies were from BioLegend. CD35-biotin antibody was from BD Biosciences. GCs were identified as IgD^- or IgD^- GL-7^+ areas. Where the number of available fluorescent channels exceeded the number of required labels, consecutive slides were stained with separate antibody panels. Images were captured using a 20× objective and a Ti2 eclipse inverted confocal microscope (Nikon). For imaging specifications, see smFISH: Hybridization and imaging. Quantification of cell number within GC DZ and LZ compartments was done using automatically detected nuclei/spots in Imaris software (v9.5.1, Oxford Instruments). Automatic threshold selection was manually verified, and non-$B220^+$ cells were removed from analysis.

Single-cell Igh sequencing

Single popliteal LNs were harvested from control and AID-$Mettl3^{fl/fl}$ mice and processed for flow cytometric analysis. Cell suspensions were stained for negative markers (dump⁻: $CD4^-$, $CD8^-$, GR-1^-, and F4/80^-) and gated as dump⁻ $B220^+$ GL-7^+ $CD38^-$ FAS^+ $IgG1^+$ or dump⁻ $B220^+$ GL-7^+ $CD38^-$ FAS^+ $IgG1^+$ IgL^+ for isolation of VH186.2-expressing cells. Cell sorting was performed using a FACS Aria II cell sorter (BD Biosciences). For total V(D)J sequencing of Ighγ1 heavy chains, GC-derived B cells were sorted into 96-well plates containing lysis buffer (PBS containing 3 U/µl ribonuclease inhibitor and 10 mM dithiothreitol). For sequencing of Ighγ1 heavy chains from VH186.2-expressing cells, GC-derived B cells were sorted in bulk into lysis/binding buffer (Life Technologies).

Single-cell total IgG sequencing and clonal analysis

Complementary DNA from single cells was generated using random primers (NEB), as previously described (Scheid et al., 2009). Ighγ1 heavy-chain sequences were amplified in a nested PCR using primers for the Ighγ1 constant region, together with a mix of primers for the variable regions (von Boehmer et al., 2016). Complementary DNA from bulk sorting was produced using qScript cDNA Synthesis Kit (QuantaBio). VH186.2 (V1-72*01) Ighγ1 heavy-chain sequences were amplified in a nested PCR using primers for the Ighγ1 constant region together with a specific primer for VH186.2 (Mayer et al., 2017; Table S1) and using high-fidelity Q5 polymerase (NEB). Amplified products were cloned (CloneJET PCR Cloning Kit, Thermo Fisher Scientific), sequenced, and analyzed.

PCR products were sequenced by Sanger sequencing, and CDR3 regions were analyzed by aligning Ig Fasta sequences against the IMGT mouse heavy gene database (September 2017) using IgBlast (v1.7.0; Ye et al., 2013). Sequence alignment was performed using SnapGene software (GSL Biotech). For a schematic representation of total Ighγ1-sequence results, sequences derived from single cells were clustered according to their CDR3 region (identical V, D, and J segment represents one clone) and presented as a fraction of total sequenced cells. Primer-derived mutations were excluded from the analysis. For schematic representation of VH186.2-sequence results, sequences were clustered according to presence/absence of W33L and K59R mutations and presented as the proportion of total sequenced cells.

Isolation of B cell mRNA

Resting B cells were isolated from mouse spleens by forcing tissue through 70-µm mesh into PBS. B cells were purified from cell suspensions using αCD43 magnetic beads (magnetic-activated cell sorting) according to the manufacturer's instructions (Miltenyi Biotec). B cell purity of ≥96% was confirmed by staining for B220 and analysis by flow cytometry. Isolated B cells were stimulated with LPS (5 mg/ml) for 1 d in vitro at 1.5×10^6 cells per ml in RPMI complete medium (10% FCS, penicillin/streptomycin, L-glutamine, Hepes, and β-mercaptoethanol). Total RNA was isolated using Trizol reagent (Invitrogen), and polyadenylated RNA was purified twice using oligo(dT) beads (Life Technologies).

M^6A-seq and analysis of m^6A methylation sites

M^6A-IP and RNA-seq library preparation were performed as previously described (Garcia-Campos et al., 2019). Three biological replicates of control and Mettl3-deficient samples were included. Reads were aligned to the mouse mm9 genome using STAR aligner (Dobin et al., 2013). A previously published approach was used to identify putative m^6A sites (Schwartz et al., 2014). Each site was assigned POI and peak over median (POM) scores representing the fold-change of enrichment in the peak region over the corresponding region in the input fraction or over the median coverage in the gene, respectively, as in Schwartz et al. (2014). For identification of sites present in the control sample but absent in the Mettl3-deficient sample, we performed wo separate *t* tests to assess whether the POM and/or POI scores differed significantly ($P < 0.05$) between control and Mettl3-deficient samples. A peak was determined to be METTL3-specific if the mean POI and mean POM scores (across the triplicates) in the control samples were higher than their counterparts in the Mettl3-deficient samples and if at least one of the two associated P values was significant. For estimating the global methylation levels per sample (Fig. S5), we calculated POI and POM scores for a preassembled set of 16,321 consistently identified m^6A

sites and a set of 30,115 control sites (Garcia-Campos et al., 2019). Sequencing data have been deposited into the NCBI Gene Expression Omnibus under accession no. GSE180359.

smFISH: Hybridization and imaging

LNs from AID-Mettl3$^{fl/+}$ and Mettl3$^{fl/fl}$ mice were extracted and fixed in 4% paraformaldehyde in ultra-clean water (Sigma-Aldrich). 5 µm (exon-only slides) or 8 µm (exon and intron slides) slices were cryo-sectioned, adhered to poly-L-lysine–treated coverslips, and washed with ice-cold 70% ethanol. Coverslips were then placed in a 6-well plate and incubated with hybridization mix overnight. Hybridization mix consisted of 10% dextran sulfate, 15% formamide, *Escherichia coli* tRNA (1 mg/ml), 2× saline sodium citrate buffer, 0.02% BSA, and 2 mM vanadyl ribonucleoside complex with both probes (1:3,000) according to a previously described protocol (Itzkovitz et al., 2012).

Probe libraries were designed and constructed as described in Raj et al. (2008). Myc intron and exon libraries consisted of 48 probes of 20-bp length, complementary to the intronic sequence or coding sequence, respectively. Ki67 libraries consisted of 96 probes (Table S3). Hybridizations were done overnight with two to three differentially labeled probes using Cy5, Alexa Fluor 594, and TMR fluorophores. A488-conjugated antibody for B220 (BioLegend) was added to the hybridization mix and used for protein immunofluorescence. 4,6-Diamidino-2-phenylindole dye for nuclear staining was added during the washes. Images were acquired with a Nikon Ti-2 inverted fluorescence microscope equipped with a 100× oil-immersion objective and a Photometrics Prime BSI scientific complementary metal oxide–semiconductor camera using NIS-Elements AR software (v5.20.01; Nikon). The image-plane pixel dimension was 0.13 µm. Quantification was done on stacks of optical sections in which not more than a single cell was observed. Dots were automatically detected using Imaris software (v9.5.1, Oxford Instruments). Automatic threshold selection was manually verified and corrected for errors. Background dots were detected according to size and by automatically identifying dots that appeared in more than one channel (typically <1% of dots) and were removed. Such dots occasionally appeared in the surrounding non-B cells but were rare in the B220$^+$ B cells. Bleed-through of transcript signal between channels was minimal. Cell segmentation was performed manually on a maximal projection of the A488 channel.

Seahorse assay

For metabolic analysis, splenic B cells were purified using negative-selection anti-CD43 magnetic beads (Miltenyi Biotec). Stimulated B cells were incubated in full RPMI with anti-IgM (10 µg/ml) overnight. Subsequently, B cells were collected, centrifuged at 300 *g* for 7 min, and resuspended in assay medium (unbuffered Seahorse RPMI, pH 7.4, supplemented with 10 mM glucose, 1 mM pyruvate, and 2 mM glutamine for the Mito assay or with 2 mM glutamine for the glyco assay). 50 µl of the cell suspensions was transferred to Cell-Tak–coated Seahorse XFe96 plates and spun at 120 *g* (0 break) for 1 min. 2.5 × 10^5 stimulated B cells or 5 × 10^5 unstimulated B cells were plated per well. Cell adhesion was evaluated using a light microscope. Before Seahorse run, cells were allowed to rest in a non-CO_2 incubator for 25 min at 37°C followed by addition of 130 µl preheated assay medium and additional 15-min incubation. A Seahorse XFe96 instrument (Agilent) was used for analysis. Additives for metabolic measurements were as follows: for oxygen consumption rate, oligomycin (1 µM), carbonyl cyanide-p trifluoromethoxyphenylhydrazone (1 µM), and rotenone/antimycin A (0.5 µM); for extracellular acidification rate, glucose (10 mM), oligomycin (1 µM), and 2-deoxyglucose (50 mM). Normalization was performed by flow cytometry–based cell counting.

Statistical analysis and reproducibility

Statistical significance was determined using GraphPad Prism v7.0 with the tests indicated in each figure.

Online supplemental material

Fig. S1 provides analysis of B cell development and early activation in METTL3-deficient B cells. Fig. S2 provides analysis of memory B cell formation, serum Ig titers, and class-switch recombination in GC B cells, as well as analysis of Cre efficiency and function of METTL3 in PPs. Fig. S3 provides immunohistochemistry analysis of DZ- and LZ-resident GC B cells in the absence of METTL3, as well as supporting results for Figs. 3 and 4. Fig. S4 provides supporting analysis of persistence of Igf2bp3-deficient GC B cells, GSEA of differential gene expression in Igf2bp3- and Ythdf2-deficient GC B cells, Seahorse metabolic analysis of ex vivo–activated Mettl3-deficient B cells, and analysis of MYC expression 3 d after mouse immunization. Fig. S5 provides additional detailed results of m^{6}A-IP experiments as well as analysis of overlap between differential gene expression and m^{6}A target genes. Fig. S5 provides description of GC identification in smFISH experiments and analysis of *Myc* mRNA stability in Igf2bp3-deficient B cells. Table S1 lists antibodies used in flow cytometry and immunohistochemistry. Table S2 lists primers used for RT-qPCR. Table S3 lists smFISH probe libraries.

Acknowledgments

This work was done with critical advice from Dr. Hadas Keren-Shaul from the Genomics Sandbox unit at the Life Science Core Facility of Weizmann Institute of Science. The graphical abstract was created with BioRender.com.

Z. Shulman is supported by European Research Council grant 101001613, Israel Science Foundation grant 1090/18, Azrieli Foundation, and the Morris Kahn Institute for Human Immunology. Z. Shulman is a member of the European Molecular Biology Organization Young Investigator Program. Z. Shulman is supported by grants from the Benoziyo Endowment Fund for the Advancement of Science, the Sir Charles Clore Research Prize, Comisaroff Family Trust, Irma & Jacques Ber-Lehmsdorf Foundation, Gerald O. Mann Charitable Foundation, and David M. Polen Charitable Trust.

Author contributions: A.C. Grenov designed and conducted the experiments, performed data analysis, and wrote the manuscript. L. Moss conducted smFISH experiments and data analysis. S. Edelheit prepared m^{6}A-seq pull-downs and libraries. R. Cordiner designed and advised on m^{6}A pull-down experiments. D. Schmiedel helped in the design and execution of some

of the experiments. A. Biram assisted in single-cell Ig sequencing and analysis. J.H. Hanna provided Mettl3-deficient mice. T.H. Jensen and S. Schwartz designed and supervised m^{6}A pull-down experiments. Z. Shulman designed experiments, supervised the study, and wrote the manuscript.

Disclosures: The authors declare no competing interests exist.

Submitted: 12 February 2021
Revised: 2 June 2021
Accepted: 22 July 2021

References

Ahmed, R., and D. Gray. 1996. Immunological memory and protective immunity: understanding their relation. *Science.* 272:54–60. https://doi.org/10.1126/science.272.5258.54

Allen, D., A. Cumano, R. Dildrop, C. Kocks, K. Rajewsky, N. Rajewsky, J. Roes, F. Sablitzky, and M. Siekevitz. 1987. Timing, genetic requirements and functional consequences of somatic hypermutation during B-cell development. *Immunol. Rev.* 96:5–22. https://doi.org/10.1111/j.1600-065X.1987.tb00506.x

Allen, C.D.C., K.M. Ansel, C. Low, R. Lesley, H. Tamamura, N. Fujii, and J.G. Cyster. 2004. Germinal center dark and light zone organization is mediated by CXCR4 and CXCR5. *Nat. Immunol.* 5:943–952. https://doi.org/10.1038/ni1100

Allen, C.D.C., T. Okada, and J.G. Cyster. 2007. Germinal-center organization and cellular dynamics. *Immunity.* 27:190–202. https://doi.org/10.1016/j.immuni.2007.07.009

Anders, S., P.T. Pyl, and W. Huber. 2015. HTSeq--a Python framework to work with high-throughput sequencing data. *Bioinformatics.* 31:166–169. https://doi.org/10.1093/bioinformatics/btu638

Bahar Halpern, K., and S. Itzkovitz. 2016. Single molecule approaches for quantifying transcription and degradation rates in intact mammalian tissues. *Methods.* 98:134–142. https://doi.org/10.1016/j.ymeth.2015.11.015

Bahar Halpern, K., S. Tanami, S. Landen, M. Chapal, L. Szlak, A. Hutzler, A. Nizhberg, and S. Itzkovitz. 2015. Bursty gene expression in the intact mammalian liver. *Mol. Cell.* 58:147–156. https://doi.org/10.1016/j.molcel.2015.01.027

Barbieri, I., K. Tzelepis, L. Pandolfini, J. Shi, G. Millán-Zambrano, S.C. Robson, D. Aspris, V. Migliori, A.J. Bannister, N. Han, et al. 2017. Promoter-bound METTL3 maintains myeloid leukaemia by m^{6}A-dependent translation control. *Nature.* 552:126–131. https://doi.org/10.1038/nature24678

Bechara, R., N. Amatya, R.D. Bailey, Y. Li, F.E.Y. Aggor, D.-D. Li, C.V. Jawale, B.M. Coleman, N. Dai, N.S. Gokhale, et al. 2021. The m6A reader IMP2 directs autoimmune inflammation through an IL-17– and TNFα-dependent C/EBP transcription factor axis. *Sci. Immunol.* 6:eabd1287. https://doi.org/10.1126/sciimmunol.abd1287

Berek, C. 1992. The development of B cells and the B-cell repertoire in the microenvironment of the germinal center. *Immunol. Rev.* 126:5–19 https://doi.org/10.1111/j.1600-065X.1992.tb00628.x

Calado, D.P., Y. Sasaki, S.A. Godinho, A. Pellerin, K. Köchert, B.P. Sleckman, I.M. de Alborán, M. Janz, S. Rodig, and K. Rajewsky. 2012. The cell-cycle regulator c-Myc is essential for the formation and maintenance of germinal centers. *Nat. Immunol.* 13:1092–1100. https://doi.org/10.1038/ni.2418

Casellas, R., U. Basu, W.T. Yewdell, J. Chaudhuri, D.F. Robbiani, and J.M. Di Noia. 2016. Mutations, kataegis and translocations in B cells: understanding AID promiscuous activity. *Nat. Rev. Immunol.* 16:164–176. https://doi.org/10.1038/nri.2016.2

Cheng, M., L. Sheng, Q. Gao, Q. Xiong, H. Zhang, M. Wu, Y. Liang, F. Zhu, Y. Zhang, X. Zhang, et al. 2019a. The m^{6}A methyltransferase METTL3 promotes bladder cancer progression via AFF4/NF-κB/MYC signaling network. *Oncogene.* 38:3667–3680. https://doi.org/10.1038/s41388-019-0683-z

Cheng, Y., H. Luo, F. Izzo, B.F. Pickering, D. Nguyen, R. Myers, A. Schurer, S. Gourkanti, J.C. Brüning, L.P. Vu, et al. 2019b. m^{6}A RNA Methylation Maintains Hematopoietic Stem Cell Identity and Symmetric Commitment. *Cell Rep.* 28:1703–1716.e6. https://doi.org/10.1016/j.celrep.2019.07.032

Chou, C., D.J. Verbaro, E. Tonc, M. Holmgren, M. Cella, M. Colonna, D. Bhattacharya, and T. Egawa. 2016. The Transcription Factor AP4 Mediates Resolution of Chronic Viral Infection through Amplification of Germinal Center B Cell Responses. *Immunity.* 45:570–582. https://doi.org/10.1016/j.immuni.2016.07.023

Corcoran, L.M., and D.M. Tarlinton. 2016. Regulation of germinal center responses, memory B cells and plasma cell formation-an update. *Curr. Opin. Immunol.* 39:59–67. https://doi.org/10.1016/j.coi.2015.12.008

Crotty, S. 2011. Follicular helper CD4 T cells (TFH). *Annu. Rev. Immunol.* 29:621–663. https://doi.org/10.1146/annurev-immunol-031210-101400

Crouch, E.E., Z. Li, M. Takizawa, S. Fichtner-Feigl, P. Gourzi, C. Montaño, L. Feigenbaum, P. Wilson, S. Janz, F.N. Papavasiliou, and R. Casellas. 2007. Regulation of AID expression in the immune response. *J. Exp. Med.* 204:1145–1156. https://doi.org/10.1084/jem.20061952

Cyster, J.G. 2010. B cell follicles and antigen encounters of the third kind. *Nat. Immunol.* 11:989–996. https://doi.org/10.1038/ni.1946

Cyster, J.G., and C.D.C. Allen. 2019. B Cell Responses: Cell Interaction Dynamics and Decisions. *Cell.* 177:524–540. https://doi.org/10.1016/j.cell.2019.03.016

Dai, N. 2020. The Diverse Functions of IMP2/IGF2BP2 in Metabolism. *Trends Endocrinol. Metab.* 31:670–679. https://doi.org/10.1016/j.tem.2020.05.007

Dani, C., J.M. Blanchard, M. Piechaczyk, S. El Sabouty, L. Marty, and P. Jeanteur. 1984. Extreme instability of myc mRNA in normal and transformed human cells. *Proc. Natl. Acad. Sci. USA.* 81:7046–7050. https://doi.org/10.1073/pnas.81.22.7046

Daniel, J.A., and A. Nussenzweig. 2013. The AID-induced DNA damage response in chromatin. *Mol. Cell.* 50:309–321. https://doi.org/10.1016/j.molcel.2013.04.017

De Silva, N.S., and U. Klein. 2015. Dynamics of B cells in germinal centres. *Nat. Rev. Immunol.* 15:137–148. https://doi.org/10.1038/nri3804

Diaz-Muñoz, M.D., S.E. Bell, K. Fairfax, E. Monzon-Casanova, A.F. Cunningham, M. Gonzalez-Porta, S.R. Andrews, V.I. Bunik, K. Zarnack, T. Curk, et al. 2015. The RNA-binding protein HuR is essential for the B cell antibody response. *Nat. Immunol.* 16:415–425. https://doi.org/10.1038/ni.3115

Dobin, A., C.A. Davis, F. Schlesinger, J. Drenkow, C. Zaleski, S. Jha, P. Batut, M. Chaisson, and T.R. Gingeras. 2013. STAR: ultrafast universal RNA-seq aligner. *Bioinformatics.* 29:15–21. https://doi.org/10.1093/bioinformatics/bts635

Dominguez-Sola, D., G.D. Victora, C.Y. Ying, R.T. Phan, M. Saito, M.C. Nussenzweig, and R. Dalla-Favera. 2012. The proto-oncogene MYC is required for selection in the germinal center and cyclic reentry. *Nat. Immunol.* 13:1083–1091. https://doi.org/10.1038/ni.2428

Dominissini, D., S. Moshitch-Moshkovitz, S. Schwartz, M. Salmon-Divon, L. Ungar, S. Osenberg, K. Cesarkas, J. Jacob-Hirsch, N. Amariglio, M. Kupiec, et al. 2012. Topology of the human and mouse m6A RNA methylomes revealed by m6A-seq. *Nature.* 485:201–206. https://doi.org/10.1038/nature11112

Du, H., Y. Zhao, J. He, Y. Zhang, H. Xi, M. Liu, J. Ma, and L. Wu. 2016. YTHDF2 destabilizes m(6)A-containing RNA through direct recruitment of the CCR4-NOT deadenylase complex. *Nat. Commun.* 7:12626. https://doi.org/10.1038/ncomms12626

Ersching, J., A. Efeyan, L. Mesin, J.T. Jacobsen, G. Pasqual, B.C. Grabiner, D. Dominguez-Sola, D.M. Sabatini, and G.D. Victora. 2017. Germinal Center Selection and Affinity Maturation Require Dynamic Regulation of mTORC1 Kinase. *Immunity.* 46:1045–1058.e6. https://doi.org/10.1016/j.immuni.2017.06.005

Finkin, S., H. Hartweger, T.Y. Oliveira, E.E. Kara, and M.C. Nussenzweig. 2019. Protein Amounts of the MYC Transcription Factor Determine Germinal Center B Cell Division Capacity. *Immunity.* 51:324–336.e5. https://doi.org/10.1016/j.immuni.2019.06.013

Furukawa, K., A. Akasako-Furukawa, H. Shirai, H. Nakamura, and T. Azuma. 1999. Junctional amino acids determine the maturation pathway of an antibody. *Immunity.* 11:329–338. https://doi.org/10.1016/S1074-7613(00)80108-9

Garcia-Campos, M.A., S. Edelheit, U. Toth, M. Safra, R. Shachar, S. Viukov, R. Winkler, R. Nir, L. Lasman, A. Brandis, et al. 2019. Deciphering the "m^{6}A Code" via Antibody-Independent Quantitative Profiling. *Cell.* 178:731–747.e16. https://doi.org/10.1016/j.cell.2019.06.013

Gitlin, A.D., Z. Shulman, and M.C. Nussenzweig. 2014. Clonal selection in the germinal centre by regulated proliferation and hypermutation. *Nature.* 509:637–640. https://doi.org/10.1038/nature13300

Gitlin, A.D., C.T. Mayer, T.Y. Oliveira, Z. Shulman, M.J.K. Jones, A. Koren, and M.C. Nussenzweig. 2015. HUMORAL IMMUNITY. T cell help controls the speed of the cell cycle in germinal center B cells. *Science.* 349:643–646. https://doi.org/10.1126/science.aac4919

Huang, C.-Y., A.L. Bredemeyer, L.M. Walker, C.H. Bassing, and B.P. Sleckman. 2008. Dynamic regulation ofc-Myc proto-oncogene expression during lymphocyte development revealed by aGFP-c-Myc knock-in mouse. *Eur. J. Immunol.* 38:342–349. https://doi.org/10.1002/eji.200737972

Huang, H., H. Weng, W. Sun, X. Qin, H. Shi, H. Wu, B.S. Zhao, A. Mesquita, C. Liu, C.L. Yuan, et al. 2018. Recognition of RNA N^6-methyladenosine by IGF2BP proteins enhances mRNA stability and translation. *Nat. Cell Biol.* 20:285–295. https://doi.org/10.1038/s41556-018-0045-z

Ise, W., and T. Kurosaki. 2019. Plasma cell differentiation during the germinal center reaction. *Immunol. Rev.* 288:64–74. https://doi.org/10.1111/imr.12751

Itzkovitz, S., A. Lyubimova, I.C. Blat, M. Maynard, J. van Es, J. Lees, T. Jacks, H. Clevers, and A. van Oudenaarden. 2012. Single-molecule transcript counting of stem-cell markers in the mouse intestine. *Nat. Cell Biol.* 14:106–114. https://doi.org/10.1038/ncb2384

Ivanova, I., C. Much, M. Di Giacomo, C. Azzi, M. Morgan, P.N. Moreira, J. Monahan, C. Carrieri, A.J. Enright, and D. O'Carroll. 2017. The RNA m^{6}A Reader YTHDF2 Is Essential for the Post-transcriptional Regulation of the Maternal Transcriptome and Oocyte Competence. *Mol. Cell.* 67:1059–1067.e4. https://doi.org/10.1016/j.molcel.2017.08.003

Jacob, J., G. Kelsoe, K. Rajewsky, and U. Weiss. 1991. Intraclonal generation of antibody mutants in germinal centres. *Nature.* 354:389–392. https://doi.org/10.1038/354389a0

Jaitin, D.A., E. Kenigsberg, H. Keren-Shaul, N. Elefant, F. Paul, I. Zaretsky, A. Mildner, N. Cohen, S. Jung, A. Tanay, and I. Amit. 2014. Massively parallel single-cell RNA-seq for marker-free decomposition of tissues into cell types. *Science.* 343:776–779. https://doi.org/10.1126/science.1247651

Jones, T.R., and M.D. Cole. 1987. Rapid cytoplasmic turnover of c-myc mRNA: requirement of the 3′ untranslated sequences. *Mol. Cell. Biol.* 7:4513–4521. https://doi.org/10.1128/MCB.7.12.4513

Keren-Shaul, H., E. Kenigsberg, D.A. Jaitin, E. David, F. Paul, A. Tanay, and I. Amit. 2019. MARS-seq2.0: an experimental and analytical pipeline for indexed sorting combined with single-cell RNA sequencing. *Nat. Protoc.* 14:1841–1862. https://doi.org/10.1038/s41596-019-0164-4

Kohen, R., J. Barlev, G. Hornung, G. Stelzer, E. Feldmesser, K. Kogan, M. Safran, and D. Leshkowitz. 2019. UTAP: User-friendly Transcriptome Analysis Pipeline. *BMC Bioinformatics.* 20:154. https://doi.org/10.1186/s12859-019-2728-2

Kwon, K., C. Hutter, Q. Sun, I. Bilic, C. Cobaleda, S. Malin, and M. Busslinger. 2008. Instructive role of the transcription factor E2A in early B lymphopoiesis and germinal center B cell development. *Immunity.* 28:751–762. https://doi.org/10.1016/j.immuni.2008.04.014

Li, H.-B., J. Tong, S. Zhu, P.J. Batista, E.E. Duffy, J. Zhao, W. Bailis, G. Cao, L. Kroehling, Y. Chen, et al. 2017. m6A mRNA methylation controls T cell homeostasis by targeting the IL-7/STAT5/SOCS pathways. *Nature.* 548:338–342. https://doi.org/10.1038/nature23450

Love, M.I., W. Huber, and S. Anders. 2014. Moderated estimation of fold change and dispersion for RNA-seq data with DESeq2. *Genome Biol.* 15:550. https://doi.org/10.1186/s13059-014-0550-8

Ma, S., J. Yan, T. Barr, J. Zhang, Z. Chen, L.-S. Wang, J.C. Sun, J. Chen, M.A. Caligiuri, and J. Yu. 2021. The RNA m6A reader YTHDF2 controls NK cell antitumor and antiviral immunity. *J. Exp. Med.* 218:e20210279. https://doi.org/10.1084/jem.20210279

MacLennan, I.C.M. 1994. Germinal centers. *Annu. Rev. Immunol.* 12:117–139. https://doi.org/10.1146/annurev.iy.12.040194.001001

Mayer, C.T., A. Gazumyan, E.E. Kara, A.D. Gitlin, J. Golijanin, C. Viant, J. Pai, T.Y. Oliveira, Q. Wang, A. Escolano, et al. 2017. The microanatomic segregation of selection by apoptosis in the germinal center. *Science.* 358:eaao2602. https://doi.org/10.1126/science.aao2602

Monzón-Casanova, E., M. Screen, M.D. Díaz-Muñoz, R.M.R. Coulson, S.E. Bell, G. Lamers, M. Solimena, C.W.J. Smith, and M. Turner. 2018. The RNA-binding protein PTBP1 is necessary for B cell selection in germinal centers. *Nat. Immunol.* 19:267–278. https://doi.org/10.1038/s41590-017-0035-5

Mootha, V.K., C.M. Lindgren, K.-F. Eriksson, A. Subramanian, S. Sihag, J. Lehar, P. Puigserver, E. Carlsson, M. Ridderstråle, E. Laurila, et al. 2003. PGC-1α-responsive genes involved in oxidative phosphorylation are coordinately downregulated in human diabetes. *Nat. Genet.* 34:267–273. https://doi.org/10.1038/ng1180

Müller, S., N. Bley, B. Busch, M. Glaß, M. Lederer, C. Misiak, T. Fuchs, A. Wedler, J. Haase, J.B. Bertoldo, et al. 2020. The oncofetal RNA-binding protein IGF2BP1 is a druggable, post-transcriptional super-enhancer of E2F-driven gene expression in cancer. *Nucleic Acids Res.* 48:8576–8590. https://doi.org/10.1093/nar/gkaa653

Palanichamy, J.K., T.M. Tran, J.M. Howard, J.R. Contreras, T.R. Fernando, T. Sterne-Weiler, S. Katzman, M. Toloue, W. Yan, G. Basso, et al. 2016. RNA-binding protein IGF2BP3 targeting of oncogenic transcripts promotes hematopoietic progenitor proliferation. *J. Clin. Invest.* 126:1495–1511. https://doi.org/10.1172/JCI80046

Pape, K.A., J.J. Taylor, R.W. Maul, P.J. Gearhart, and M.K. Jenkins. 2011. Different B cell populations mediate early and late memory during an endogenous immune response. *Science.* 331:1203–1207. https://doi.org/10.1126/science.1201730

Plotkin, S.A. 2008. Vaccines: correlates of vaccine-induced immunity. *Clin. Infect. Dis.* 47:401–409. https://doi.org/10.1086/589862

Raj, A., P. van den Bogaard, S.A. Rifkin, A. van Oudenaarden, and S. Tyagi. 2008. Imaging individual mRNA molecules using multiple singly labeled probes. *Nat. Methods.* 5:877–879. https://doi.org/10.1038/nmeth.1253

Ren, F., Q. Lin, G. Gong, X. Du, H. Dan, W. Qin, R. Miao, Y. Xiong, R. Xiao, X. Li, et al. 2020. Igf2bp3 maintains maternal RNA stability and ensures early embryo development in zebrafish. *Commun. Biol.* 3:94. https://doi.org/10.1038/s42003-020-0827-2

Roco, J.A., L. Mesin, S.C. Binder, C. Nefzger, P. Gonzalez-Figueroa, P.F. Canete, J. Ellyard, Q. Shen, P.A. Robert, J. Cappello, et al. 2019. Class-Switch Recombination Occurs Infrequently in Germinal Centers. *Immunity.* 51:337–350.e7. https://doi.org/10.1016/j.immuni.2019.07.001

Rommel, P.C., D. Bosque, A.D. Gitlin, G.F. Croft, N. Heintz, R. Casellas, M.C. Nussenzweig, S. Kriaucionis, and D.F. Robbiani. 2013. Fate mapping for activation-induced cytidine deaminase (AID) marks non-lymphoid cells during mouse development. *PLoS One.* 8:e69208. https://doi.org/10.1371/journal.pone.0069208

Samuels, T.J., A.I. Järvelin, D. Ish-Horowicz, and I. Davis. 2020. Imp/IGF2BP levels modulate individual neural stem cell growth and division through *myc* mRNA stability. *eLife.* 9:e51529. https://doi.org/10.7554/eLife.51529

Sander, S., D.P. Calado, L. Srinivasan, K. Köchert, B. Zhang, M. Rosolowski, S.J. Rodig, K. Holzmann, S. Stilgenbauer, R. Siebert, et al. 2012. Synergy between PI3K signaling and MYC in Burkitt lymphomagenesis. *Cancer Cell.* 22:167–179. https://doi.org/10.1016/j.ccr.2012.06.012

Scheid, J.F., H. Mouquet, N. Feldhahn, B.D. Walker, F. Pereyra, E. Cutrell, M.S. Seaman, J.R. Mascola, R.T. Wyatt, H. Wardemann, and M.C. Nussenzweig. 2009. A method for identification of HIV gp140 binding memory B cells in human blood. *J. Immunol. Methods.* 343:65–67. https://doi.org/10.1016/j.jim.2008.11.012

Schwartz, S., M.R. Mumbach, M. Jovanovic, T. Wang, K. Maciag, G.G. Bushkin, P. Mertins, D. Ter-Ovanesyan, N. Habib, D. Cacchiarelli, et al. 2014. Perturbation of m6A writers reveals two distinct classes of mRNA methylation at internal and 5′ sites. *Cell Rep.* 8:284–296. https://doi.org/10.1016/j.celrep.2014.05.048

Schwickert, T.A., G.D. Victora, D.R. Fooksman, A.O. Kamphorst, M.R. Mugnier, A.D. Gitlin, M.L. Dustin, and M.C. Nussenzweig. 2011. A dynamic T cell-limited checkpoint regulates affinity-dependent B cell entry into the germinal center. *J. Exp. Med.* 208:1243–1252. https://doi.org/10.1084/jem.20102477

Shi, H., X. Wang, Z. Lu, B.S. Zhao, H. Ma, P.J. Hsu, C. Liu, and C. He. 2017. YTHDF3 facilitates translation and decay of N^6-methyladenosine-modified RNA. *Cell Res.* 27:315–328. https://doi.org/10.1038/cr.2017.15

Shi, H., J. Wei, and C. He. 2019. Where, When, and How: Context-Dependent Functions of RNA Methylation Writers, Readers, and Erasers. *Mol. Cell.* 74:640–650. https://doi.org/10.1016/j.molcel.2019.04.025

Shlomchik, M.J., and F. Weisel. 2012. Germinal center selection and the development of memory B and plasma cells. *Immunol. Rev.* 247:52–63. https://doi.org/10.1111/j.1600-065X.2012.01124.x

Shulman, Z., and N. Stern-Ginossar. 2020. The RNA modification N^6-methyladenosine as a novel regulator of the immune system. *Nat. Immunol.* 21:501–512. https://doi.org/10.1038/s41590-020-0650-4

Stewart, I., D. Radtke, B. Phillips, S.J. McGowan, and O. Bannard. 2018. Germinal Center B Cells Replace Their Antigen Receptors in Dark Zones and Fail Light Zone Entry when Immunoglobulin Gene Mutations are Damaging. *Immunity.* 49:477–489.e7. https://doi.org/10.1016/j.immuni.2018.08.025

Subramanian, A., P. Tamayo, V.K. Mootha, S. Mukherjee, B.L. Ebert, M.A. Gillette, A. Paulovich, S.L. Pomeroy, T.R. Golub, E.S. Lander, and J.P. Mesirov. 2005. Gene set enrichment analysis: a knowledge-based approach for interpreting genome-wide expression profiles. *Proc. Natl. Acad. Sci. USA.* 102:15545–15550. https://doi.org/10.1073/pnas.0506580102

Sun, L., F.M. Fazal, P. Li, J.P. Broughton, B. Lee, L. Tang, W. Huang, E.T. Kool, H.Y. Chang, and Q.C. Zhang. 2019. RNA structure maps across mammalian cellular compartments. *Nat. Struct. Mol. Biol.* 26:322–330. https://doi.org/10.1038/s41594-019-0200-7

Tarlinton, D., and K. Good-Jacobson. 2013. Diversity among memory B cells: origin, consequences, and utility. *Science.* 341:1205–1211. https://doi.org/10.1126/science.1241146

Turner, M., and M.D. Díaz-Muñoz. 2018. RNA-binding proteins control gene expression and cell fate in the immune system. *Nat. Immunol.* 19: 120–129. https://doi.org/10.1038/s41590-017-0028-4

Vander Heiden, M.G., L.C. Cantley, and C.B. Thompson. 2009. Understanding the Warburg effect: the metabolic requirements of cell proliferation. *Science.* 324:1029–1033. https://doi.org/10.1126/science.1160809

Victora, G.D., and M.C. Nussenzweig. 2012. Germinal centers. *Annu. Rev. Immunol.* 30:429–457. https://doi.org/10.1146/annurev-immunol-020711-075032

Victora, G.D., T.A. Schwickert, D.R. Fooksman, A.O. Kamphorst, M. Meyer-Hermann, M.L. Dustin, and M.C. Nussenzweig. 2010. Germinal center dynamics revealed by multiphoton microscopy with a photoactivatable fluorescent reporter. *Cell.* 143:592–605. https://doi.org/10.1016/j.cell.2010.10.032

Vinuesa, C.G., and J.G. Cyster. 2011. How T cells earn the follicular rite of passage. *Immunity.* 35:671–680. https://doi.org/10.1016/j.immuni.2011.11.001

von Boehmer, L., C. Liu, S. Ackerman, A.D. Gitlin, Q. Wang, A. Gazumyan, and M.C. Nussenzweig. 2016. Sequencing and cloning of antigen-specific antibodies from mouse memory B cells. *Nat. Protoc.* 11:1908–1923. https://doi.org/10.1038/nprot.2016.102

Vu, L.P., B.F. Pickering, Y. Cheng, S. Zaccara, D. Nguyen, G. Minuesa, T. Chou, A. Chow, Y. Saletore, M. MacKay, et al. 2017. The N^6-methyladenosine (m^{6}A)-forming enzyme METTL3 controls myeloid differentiation of normal hematopoietic and leukemia cells. *Nat. Med.* 23:1369–1376. https://doi.org/10.1038/nm.4416

Wang, X., Z. Lu, A. Gomez, G.C. Hon, Y. Yue, D. Han, Y. Fu, M. Parisien, Q. Dai, G. Jia, et al. 2014. N6-methyladenosine-dependent regulation of messenger RNA stability. *Nature.* 505:117–120. https://doi.org/10.1038/nature12730

Weidensdorfer, D., N. Stöhr, A. Baude, M. Lederer, M. Köhn, A. Schierhorn, S. Buchmeier, E. Wahle, and S. Hüttelmaier. 2009. Control of c-myc mRNA stability by IGF2BP1-associated cytoplasmic RNPs. *RNA.* 15: 104–115. https://doi.org/10.1261/rna.1175909

Weisel, F.J., S.J. Mullett, R.A. Elsner, A.V. Menk, N. Trivedi, W. Luo, D. Wikenheiser, W.F. Hawse, M. Chikina, S. Smita, et al. 2020. Germinal center B cells selectively oxidize fatty acids for energy while conducting minimal glycolysis. *Nat. Immunol.* 21:331–342. https://doi.org/10.1038/s41590-020-0598-4

Weng, H., H. Huang, H. Wu, X. Qin, B.S. Zhao, L. Dong, H. Shi, J. Skibbe, C. Shen, C. Hu, et al. 2018. METTL14 Inhibits Hematopoietic Stem/Progenitor Differentiation and Promotes Leukemogenesis via mRNA m^{6}A Modification. *Cell Stem Cell.* 22:191–205.e9. https://doi.org/10.1016/j.stem.2017.11.016

Yao, Y., Y. Yang, W. Guo, L. Xu, M. You, Y.-C. Zhang, Z. Sun, X. Cui, G. Yu, Z. Qi, et al. 2021. METTL3-dependent m6A modification programs T follicular helper cell differentiation. *Nat Commun.* 12:1333. https://doi.org/10.1038/s41467-021-21594-6

Ye, J., N. Ma, T.L. Madden, and J.M. Ostell. 2013. IgBLAST: an immunoglobulin variable domain sequence analysis tool. *Nucleic Acids Res.* 41(W1): W34–40. https://doi.org/10.1093/nar/gkt382

Youn, J.-Y., W.H. Dunham, S.J. Hong, J.D.R. Knight, M. Bashkurov, G.I. Chen, H. Bagci, B. Rathod, G. MacLeod, S.W.M. Eng, et al. 2018. High-Density Proximity Mapping Reveals the Subcellular Organization of mRNA-Associated Granules and Bodies. *Mol. Cell.* 69:517–532.e11. https://doi.org/10.1016/j.molcel.2017.12.020

Zaccara, S., and S.R. Jaffrey. 2020. A Unified Model for the Function of YTHDF Proteins in Regulating m^{6}A-Modified mRNA. *Cell.* 181: 1582–1595.e18. https://doi.org/10.1016/j.cell.2020.05.012

Zaccara, S., R.J. Ries, and S.R. Jaffrey. 2019. Reading, writing and erasing mRNA methylation. *Nat. Rev. Mol. Cell Biol.* 20:608–624. https://doi.org/10.1038/s41580-019-0168-5

Zaretsky, I., O. Atrakchi, R.D. Mazor, L. Stoler-Barak, A. Biram, S.W. Feigelson, A.D. Gitlin, B. Engelhardt, and Z. Shulman. 2017. ICAMs support B cell interactions with T follicular helper cells and promote clonal selection. *J. Exp. Med.* 214:3435–3448. https://doi.org/10.1084/jem.20171129

Zhang, C., L. Chen, D. Peng, A. Jiang, Y. He, Y. Zeng, C. Xie, H. Zhou, X. Luo, H. Liu, et al. 2020. METTL3 and N6-Methyladenosine Promote Homologous Recombination-Mediated Repair of DSBs by Modulating DNA-RNA Hybrid Accumulation. *Mol. Cell.* 79:425–442.e7. https://doi.org/10.1016/j.molcel.2020.06.017

Zhang, Y., M. Meyer-Hermann, L.A. George, M.T. Figge, M. Khan, M. Goodall, S.P. Young, A. Reynolds, F. Falciani, A. Waisman, et al. 2013. Germinal center B cells govern their own fate via antibody feedback. *J. Exp. Med.* 210:457–464. https://doi.org/10.1084/jem.20120150

Zhao, W., Y. Cui, L. Liu, X. Ma, X. Qi, Y. Wang, Z. Liu, S. Ma, J. Liu, and J. Wu. 2020. METTL3 Facilitates Oral Squamous Cell Carcinoma Tumorigenesis by Enhancing c-Myc Stability via YTHDF1-Mediated m^{6}A Modification. *Mol. Ther. Nucleic Acids.* 20:1–12. https://doi.org/10.1016/j.omtn.2020.01.033

Zheng, Z., L. Zhang, X.-L. Cui, X. Yu, P.J. Hsu, R. Lyu, H. Tan, M. Mandal, M. Zhang, H.L. Sun, et al. 2020. Control of Early B Cell Development by the RNA N^6-Methyladenosine Methylation. *Cell Rep.* 31:107819. https://doi.org/10.1016/j.celrep.2020.107819

Zhou, Y., B. Zhou, L. Pache, M. Chang, A.H. Khodabakhshi, O. Tanaseichuk, C. Benner, and S.K. Chanda. 2019. Metascape provides a biologist-oriented resource for the analysis of systems-level datasets. *Nat. Commun.* 10: 1523. https://doi.org/10.1038/s41467-019-09234-6

JEM

Supplemental material

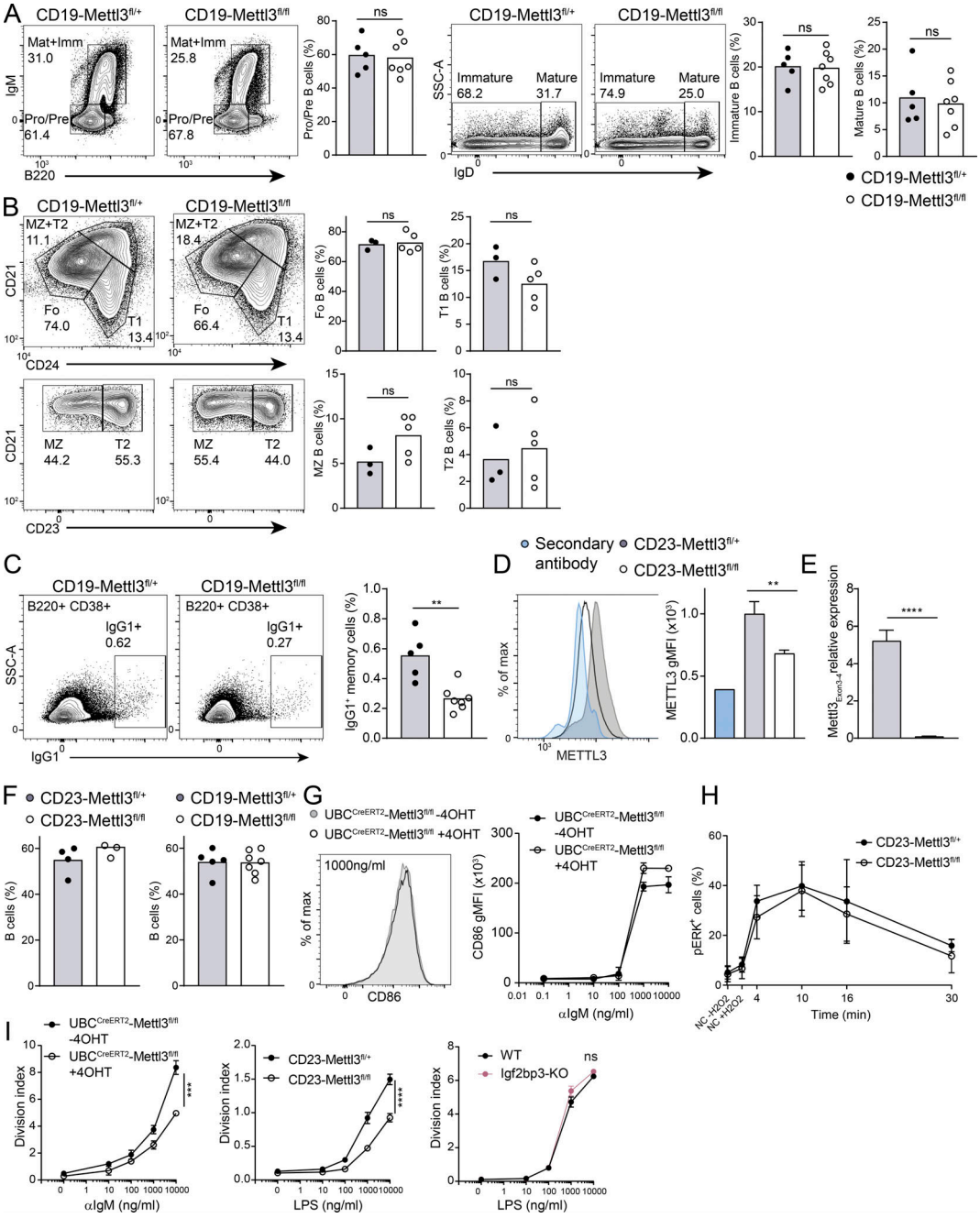

Figure S1. **B cell homeostasis and early activation does not depend on METTL3. (A and B)** Flow cytometry analysis of B cell developmental stages in the BM (A) and spleen (B). Pooled data from two to three experiments with a total of five to seven mice per group. Each data point represents a single mouse, and column heights represent mean values. SSC, side scatter. **(C)** CD19-Mettl3$^{fl/+}$ or CD19-Mettl3$^{fl/fl}$ mice were immunized in the footpad with NP-KLH. After 7 d, the relative numbers of CD38$^+$ IgG1$^+$ memory B cells were examined by flow cytometry. Data pooled from three experiments with five to seven mice per condition in total. **(D and E)** Unmanipulated splenic cells from CD23-Mettl3$^{fl/fl}$ and control mice were stained intracellularly with polyclonal METTL3 antibody and either analyzed by flow cytometry (D) or subjected to RT-qPCR for the floxed exon 3–4 (E). Column height represents mean + SD (B) or SEM (C). Pooled data from one (D) or two (C) experiments with a total of three to five mice per group. **(F)** Popliteal LN cell suspensions from CD19-Cre and CD23-Cre Mettl3$^{fl/fl}$ and control mice were analyzed for percentage of B220 B cells by flow cytometry. Data pooled from two experiments with a total of three to seven mice per group. **(G)** UBC^{CreERT2}-Mettl3fl/fl splenic B cells were treated with or without 4OHT for 24 h and then washed and stimulated with anti-IgM overnight, followed by analysis of CD86 expression by flow cytometry. Plots are representative of two independent experiments performed with triplicate samples. Points indicate mean + SD. **(H)** Isolated B cells from CD23-Mettl3$^{fl/fl}$ and control mice were stimulated with 10 µg anti-IgM for 0–30 min in the presence of 0.4 mM H_2O_2 and stained intracellularly with anti-pERK. Pooled data from three independent experiments. Points indicate mean + SD. NC, negative control **(I)** Splenocytes derived from UBC^{CreERT2}-Mettl3$^{fl/fl}$, CD23-Mettl3$^{fl/fl}$, and CD23-Mettl3$^{fl/+}$ or Igf2bp3$^{-/-}$ and WT mice were stained with CellTrace Violet and stimulated with LPS or anti-IgM for 3 d in vitro. Quantification of the B cell division index of two to four experiments performed with triplicate samples are shown. Splenic cells from UBC^{CreERT2}-Mettl3$^{fl/fl}$ mice were treated with or without 4OHT for 24 h before stimulation. Unpaired Student's *t* test (A–C and E), one-way ANOVA (D), or two-way ANOVA (G–I) with multiple comparisons (Holm–Sidak one-way, Sidak two-way) were used to determine significance. **, P < 0.01; ***, P < 0.005; ****, P < 0.001.

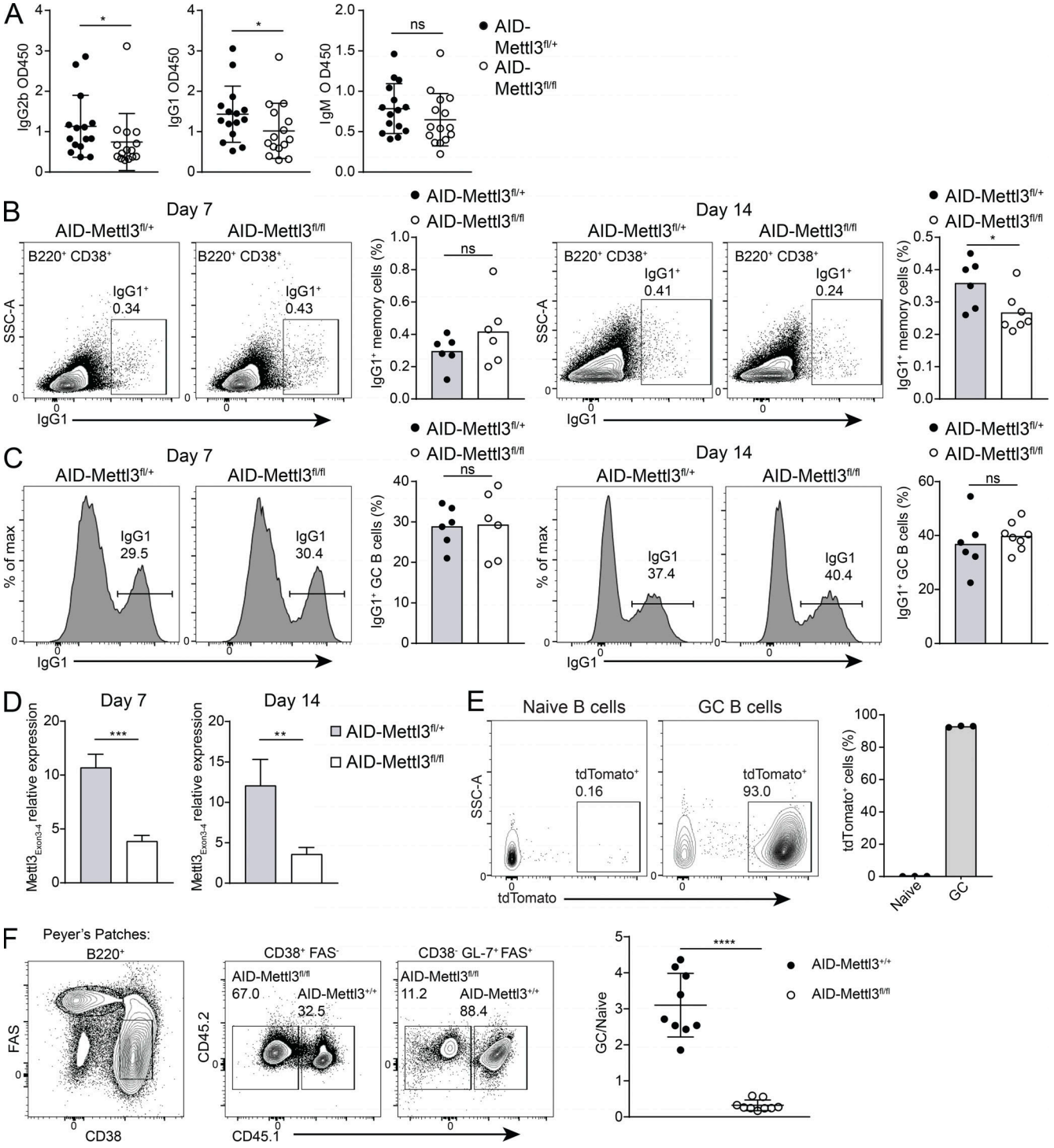

Figure S2. **METTL3 is required for memory and GC B cell formation but not for isotype class switch recombination. (A)** Serum Ig titers in AID-Mettl3$^{fl/+}$ or AID-Mettl3$^{fl/fl}$ mice. 15 mice per condition; significance was determined using Student's paired *t* test between age-matched mice. **(B and C)** AID-Mettl3$^{fl/+}$ or AID-Mettl3$^{fl/fl}$ mice were immunized with NP-KLH in the footpad. After 7 and 14 d, the relative numbers of CD38$^+$ IgG1$^+$ memory B cells (B) and IgG1$^+$ B cells (C) were quantified by flow cytometry. Results show pooled data from three experiments with a total of six mice per group. SSC, side scatter. **(D)** Mettl3 mRNA expression in GC B cells determined by RT-qPCR for exon 3-4 of Mettl3 in AID-Mettl3$^{fl/fl}$ and control cells. Data represent one experiment with five mice per group. **(E)** TdTomato expression in AID-Cre R26$^{stop\text{-}TdTomato\text{-}stop}$ mice. Data represent one experiment with three mice per group. **(F)** Chimeric mice were generated by transfer of a mixture of cells containing 30% control BM cells (AID$^{cre/+}$) and 70% AID-Mettl3$^{fl/fl}$ BM cells. The frequency of GC cells in PPs of control and AID-Mettl3$^{fl/fl}$ cells was examined by flow cytometry. Pooled data from three experiments with two to three mice per group. Column heights represent mean (B–D), and lines indicate mean + SD (A and F). Unpaired Student's *t* test (B–F) was used to determine significance. *, P < 0.05; **, P < 0.01; ***, P < 0.005; ****, P < 0.001.

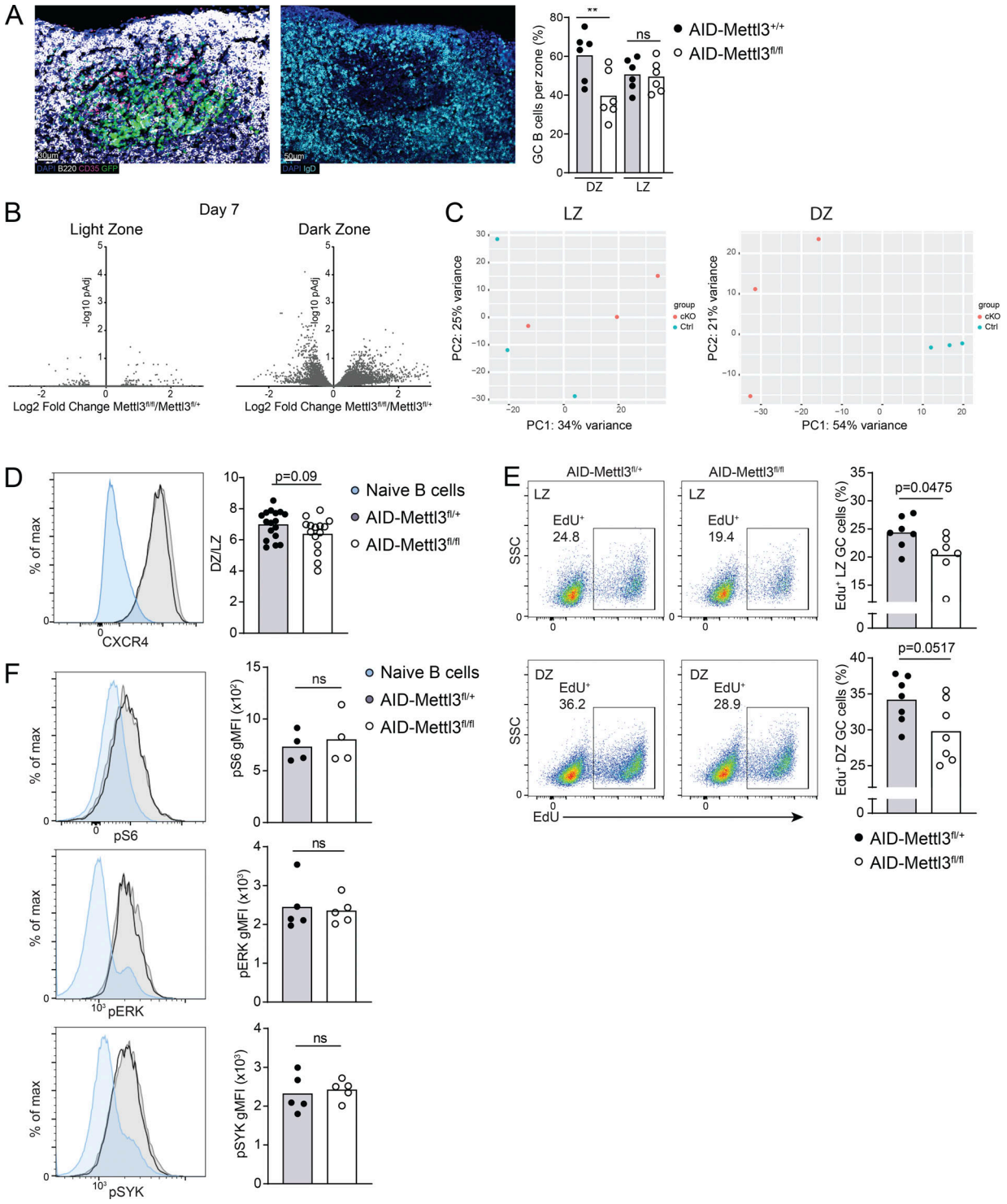

Figure S3. **METTL3 regulates the DZ compartment in GCs but not BCR signaling. (A)** Chimeric mice were generated by transfer of a mixture of cells containing 50% control BM cells (AID$^{cre/+}$ GFP) and 50% AID-Mettl3$^{fl/fl}$ BM cells. 14 d after immunization with NP-KLH, GCs were analyzed by immunohistochemistry. The distribution of Mettl3-deficient and control cells within the DZ and LZ was determined by staining with B220 (B cells), IgD (GCs), and CD35 (follicular dendritic cells). The plot shows pooled results from 2 mice, 4 popliteal LNs, and 498 (DZ) and 481 (LZ) cells. **(B and C)** Additional supporting results for the experiments shown in Fig. 3B and corresponding text. Differential gene expression of control and Mettl3-deficient cells 7 d after immunization with NP-KLH (B) and 14 d after immunization by principal component (PC) analysis plot (C). **(D)** CXCR4 expression analyzed by flow cytometry in control and AID-Mettl3$^{fl/fl}$ GC B cells 14 d after immunization. Data pooled from five experiments with a total of 15–17 mice per group. **(E)** Supporting results for Fig. 4 A. EdU incorporation in GC DZ and LZ B cells, respectively. **(F)** Anti-pS6, pERK, and pSYK staining in control and Mettl3-deficient GC B cells as measured by flow cytometry. Dots represent individual mice, and column height represents the mean. Pooled data from two experiments with a total of four to five mice per group. SSC, side scatter. Statistical significance determined by unpaired Student's *t* test (D–F) or one-way ANOVA with Holm–Sidak's multiple comparisons test (A). **, P < 0.01.

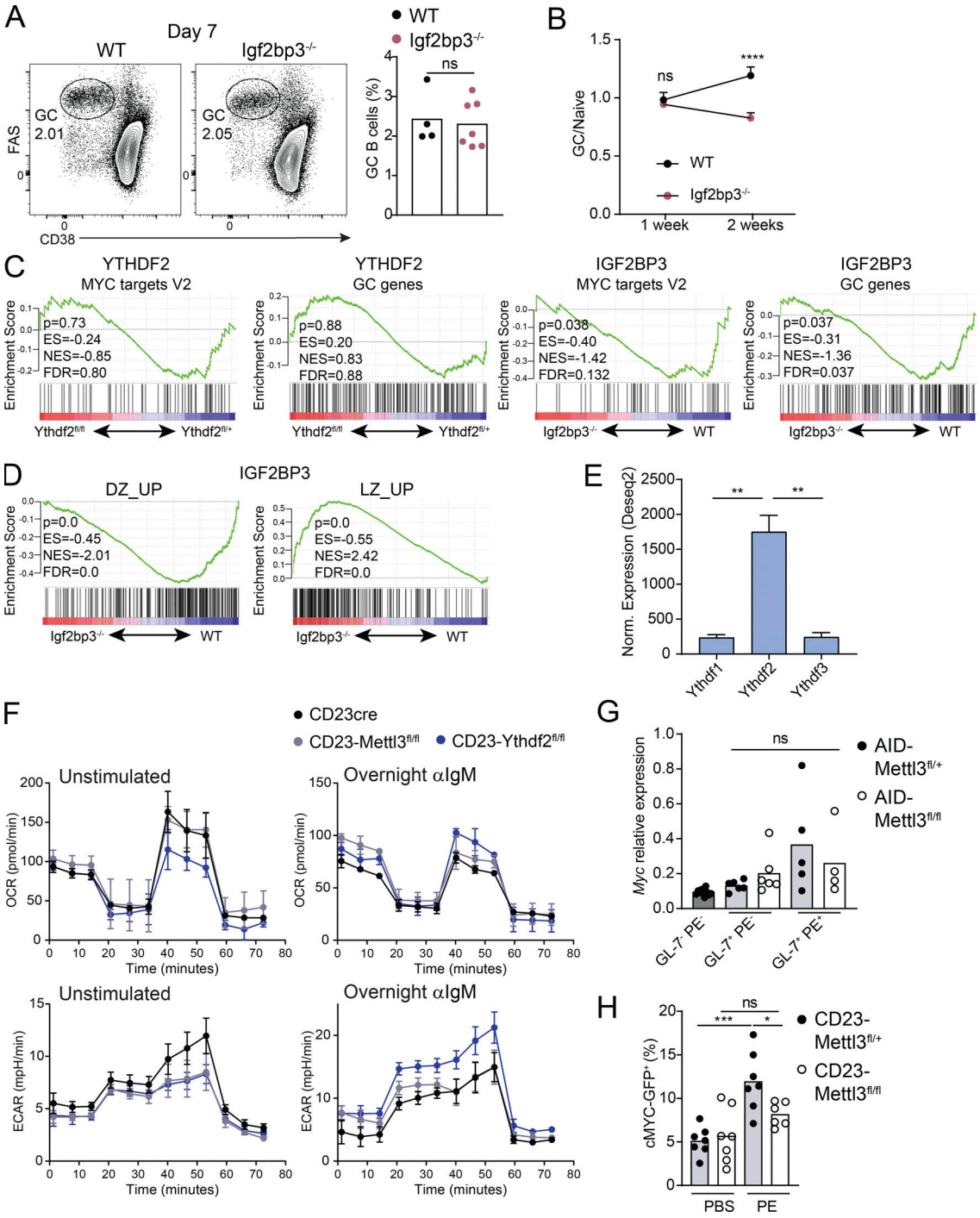

Figure S4. **IGF2BP3 and YTHDF2 regulate different gene signatures in GC B cells. (A)** The frequency of GC cells in WT and Igf2bp3$^{-/-}$ mice 7 d after immunization. Data pooled from three experiments with a total of four to seven mice per group. **(B)** Chimeric mice generated by BM transfer of 30% WT and 70% Igf2bp3$^{-/-}$ cells were analyzed for the fraction of each cell type in the naive and GC B cell compartments 1 and 2 wk after immunization with NP-KLH. Pooled data from three experiments, each with three to four mice. Each data point represents mean + SD. **(C)** Additional supporting results from the experiments shown in Fig. 5, B and D. GSEA of GC B cells derived from Ythdf2- and Igf2bp3-deficient and control mice. **(D)** GSEA plots of DZ and LZ gene signatures in Igf2bp3$^{-/-}$ versus WT GC B cells. **(E)** Analysis of YTHDF1/2/3 expression in RNA-seq data of GC B cells based on dataset GSE98778. Norm., normalized. **(F)** Metabolic capacity of unstimulated and stimulated (anti-IgM overnight) isolated B cells from control, CD23-Mettl3$^{fl/fl}$, and CD23-Ythdf2$^{fl/fl}$ mice was measured in a Seahorse assay. Plots are representative of two to three independent experiments with three replicates in each. Points indicate mean + SD. ECAR, extracellular acidification rate; OCR, oxygen consumption rate. **(G)** PE- and GL-7–positive and -negative populations were sorted from AID-Mettl3$^{fl/fl}$ and control mice 3 d after immunization with PE. RT-qPCR was used to determine *Myc* mRNA levels in each population. Plot shows pooling of two independent experiments. **(H)** Analysis of cMYC-GFP expression in CD23-Mettl3$^{fl/fl}$ and CD23-Mettl3$^{fl/+}$ PE^{+} B cells 3 d after PBS or PE immunization. Plot shows pooling of three experiments with two to three mice per group. One datapoint >2 SD from mean was removed from group D. Statistical significance was determined by unpaired Student's *t* test (A), one-way ANOVA (E, G, and H), or two-way ANOVA (B) with Holm–Sidak's (one-way) or Sidak's (two-way) multiple comparisons test. *, P < 0.05; **, P < 0.01; ***, P < 0.005; ****, P < 0.001.

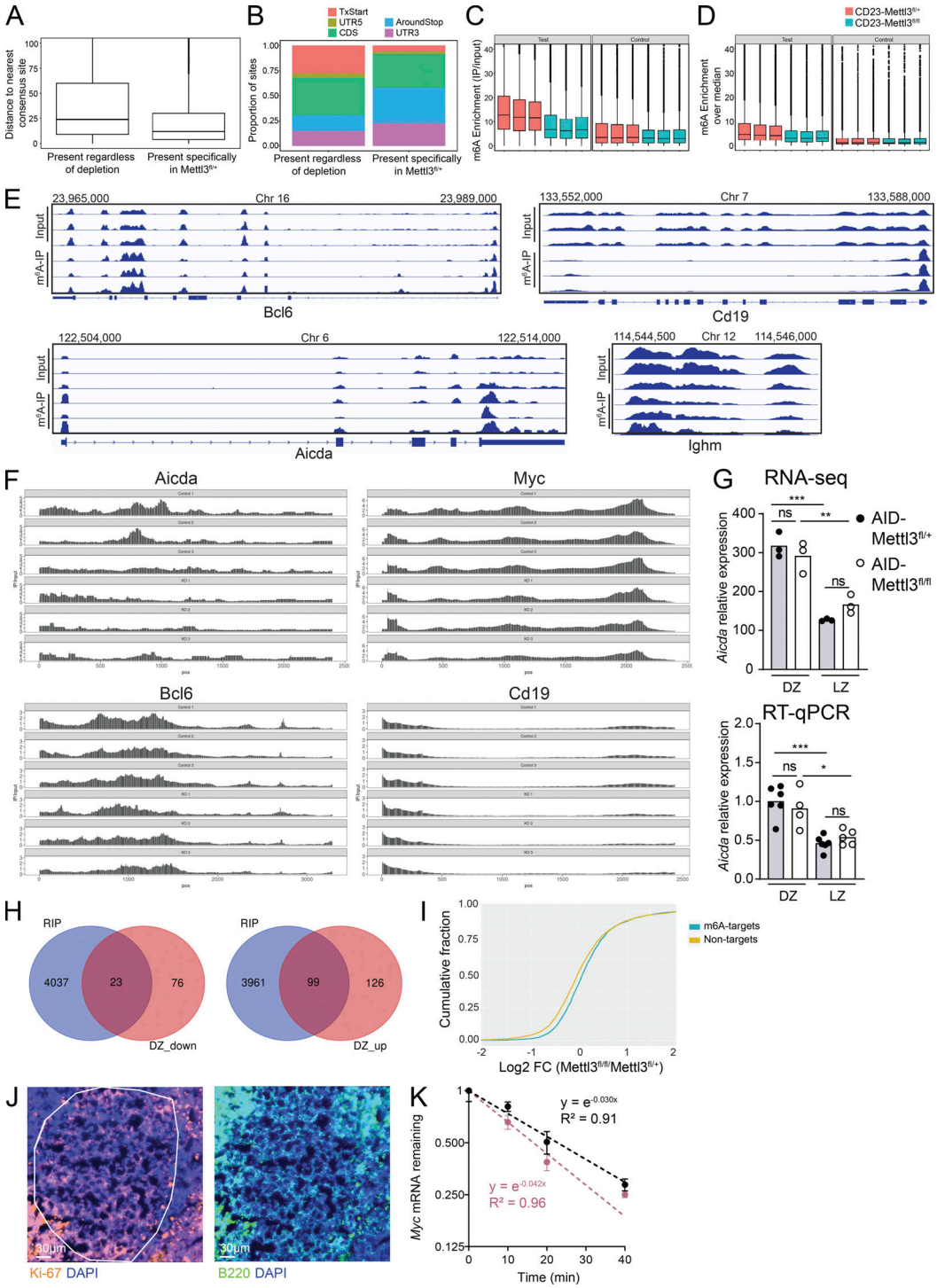

Figure S5. **B cells derived from Mettl3-deficient mice show decreased levels of m^{6}A methylation. (A)** Analysis of m^{6}A abundance in B cells that were stimulated with LPS in vitro. Distributions of distance from the nearest consensus site, of sites that are present only in control samples, or both control and Mettl3-deficient B cells. **(B)** Distribution of the sites in A grouped across five gene segments as defined in Dominissini et al. (2012). **(C and D)** Calculated POI (C) and POM (D) scores for control and Mettl3-deficient B cells. **(E and F)** Examples of m^{6}A methylation sites in B cell–related genes. Input and m^{6}A results are shown separately (E) or as a ratio of IP/Input for control and CD23-Mettl3$^{fl/fl}$ B cells (F). **(G)** Aicda mRNA expression as measured by MARS-seq (top) and RT-qPCR (bottom) in GC B cells sorted from immunized control and AID-Mettl3$^{fl/fl}$ mice 14 d after immunization. Pooled data from two experiments with a total of three to six mice per group. Statistical significance determined using one-way ANOVA with Holm–Sidak's multiple comparisons test. **(H)** Venn diagrams showing the overlap between m6A targets (in LPS-stimulated B cells) and significantly differentially expressed genes (between AID-Mettl3$^{fl/fl}$ and AID-Mettl3$^{fl/+}$ DZ B cells) day 14 after immunization. RIP, RNA immunoprecipitation. **(I)** Cumulative frequency of mRNA log2 fold-change (FC) in nontarget and m^{6}A-IP target genes upon Mettl3 deletion in DZ GC B cells. **(J)** Additional supporting results from experiments shown in Fig. 7, C–E. Identification of GC B cells by staining for Ki-67 mRNA (smFISH) and B220 (antibody labeling). **(K)** *Myc* mRNA stability assay in B cells isolated from WT and Igf2bp3$^{-/-}$ mice. Transcription was stopped using actinomycin D, and *Myc* mRNA levels were measured at increasing time points by RT-qPCR. *, P < 0.05; **, P < 0.01; ***, P < 0.005.

Provided online are three tables. Table S1 lists antibodies used in flow cytometry. Table S2 lists primers for RT-qPCR. Table S3 provides a list of smFISH probe libraries.